



# Study of low concentration CO poisoning of Pt anode in a proton exchange membrane fuel cell using spatial electrochemical impedance spectroscopy



Tatyana V. Reshetenko<sup>a,\*</sup>, Keith Bethune<sup>a</sup>, Miguel A. Rubio<sup>b</sup>, Richard Rocheleau<sup>a</sup>

<sup>a</sup> Hawaii Natural Energy Institute, University of Hawaii, 1680 East-West Road, POST 109, Honolulu, HI 96822, USA

<sup>b</sup> Departamento de Informática y Automática, UNED, Juan del Rosal 16, 28040 Madrid, Spain

## HIGHLIGHTS

- The effects of CO on spatial PEMFC performance and EIS were studied with a segmented cell.
- The experiments were performed using various cathode gases: air, O<sub>2</sub> and H<sub>2</sub>.
- Injection of CO resulted in a voltage decrease and redistribution of segments' currents.
- The spatial EIS data were analyzed using the equivalent electric circuits approach.
- A current distribution model and EIS interpolation method were applied for detailed analysis.

## ARTICLE INFO

### Article history:

Received 22 April 2014

Received in revised form

25 June 2014

Accepted 26 June 2014

Available online 7 July 2014

### Keywords:

PEMFC

Pt anode

Carbon monoxide poisoning

Spatial EIS

## ABSTRACT

This paper presents experimental and modeling results of the effect of low CO concentration (2 ppm) on the spatial performance of PEMFC as well as its spatial electrochemical impedance spectroscopy (EIS) responses. The cell was operated at constant current using various cathode gases: air, O<sub>2</sub> and H<sub>2</sub>. Due to CO adsorption on the Pt anode and its poisoning, the cell voltage decreased and spatial current redistribution was observed. The steady state voltage losses were 0.089, 0.280 and 0.295 V for the H<sub>2</sub>/O<sub>2</sub>, H<sub>2</sub>/air and H<sub>2</sub>/H<sub>2</sub> gas configurations, respectively. EIS data revealed a pseudo-inductive behavior in the low frequency region for inlet segments of the cell operated under H<sub>2</sub>/air and H<sub>2</sub>/H<sub>2</sub> conditions. Operation with O<sub>2</sub> as an oxidant did not cause any pseudo-inductance. Analysis of the EIS and anode overpotential data suggested that CO oxidation occurred via chemical or electrochemical mechanisms, or a combination of both depending on the selected cathode gas. The spatial EIS data were analyzed using the equivalent electric circuits approach. The distributions of the equivalent electric circuit parameters are presented and discussed. A current distribution model and EIS interpolation technique were successfully applied for detailed analysis of CO effects on the spatial PEMFC performance and EIS.

© 2014 Elsevier B.V. All rights reserved.

## 1. Introduction

Fuel cells are receiving increasing attention due to their high energy conversion rates and harmless emission products as well as their promising future applications for powering stationary and portable devices and electric vehicles [1]. The highest performance is achieved with H<sub>2</sub>, which is the preferred fuel for low temperature proton exchange membrane fuel cells (PEMFCs). However, the

application of H<sub>2</sub> as a fuel for PEMFCs has several limitations, predominantly due to current methods of H<sub>2</sub> production which commonly occurs via the steam reforming of natural gas [2,3] as well as water electrolysis. Focusing on the reforming processes, a by-product of these is carbon monoxide. To minimize the CO content, several additional stages are incorporated into the reforming process, namely the water gas shift reaction and low temperature preferential oxidation. The resulting CO concentration is in the range of 10–50 ppm. However, even a low CO content can significantly reduce the performance of fuel cells [4–17]. Recent standards released specifying acceptable hydrogen gas compositions for fuel cell applications set the maximum CO concentration at 0.2 ppm in attempt to alleviate concerns of contamination (ISO

\* Corresponding author. Tel.: +1 808 593 1714; fax: +1 808 593 1719.

E-mail addresses: [tatyanar@hawaii.edu](mailto:tatyanar@hawaii.edu), [treshetenko@mail.ru](mailto:treshetenko@mail.ru) (T.V. Reshetenko).

14687–2, SAE J2719). The main reason for the performance loss due to CO contamination in PEMFCs is the preferential adsorption of CO on Pt sites, which leads to the inhibition of H<sub>2</sub> dissociative adsorption and its further oxidation. Several approaches have been proposed to mitigate the effect of CO on PEMFCs. These approaches include preventative measures by reducing carbon monoxide concentrations through current advances in preferential CO oxidation techniques and the water gas shift reaction [1–3,18], and in-situ techniques such as the pulsed oxidation of a CO poisoned electrode [19,20], air bleeding into a H<sub>2</sub> stream [3,4,13,21–25], the use of CO-tolerant catalysts [7,10,11,23,26,27], and/or operation under particular conditions (high temperature, pure H<sub>2</sub> pulsing, high cathode back pressure) [28–31].

For the diagnosis of fuel cell performance, electrochemical impedance spectroscopy (EIS) is a well-established method [32–35]. The method is based on a small sinusoidal perturbation of the electrochemical system (either in current or voltage) and measurement of the response signal. Because of the small amplitude of the perturbation, the system is assumed to be linear in the range of perturbation, and the linear impedance is analyzed. Variation of the perturbation frequency allows processes with different time constants to be separated. EIS has been applied for the investigation of various phenomena in PEMFC: dehydration, flooding and poisoning by impurities including CO.

The first in-situ measurements of CO poisoning with EIS were published by B. Müller [36] and M. Ciureanu [37]. The paper [36] reported the time dependence of impedance spectra under galvanostatic conditions and CO exposure of the Pt anode, while potentiostatic electro-oxidation of H<sub>2</sub>/CO was studied in Ref. [37]. It is useful to operate the fuel cell in the galvanostatic mode because a constant current density means a constant reaction rate. Additionally, the impedance of the membrane and cathode might also be assumed to be constant, and any observed differences in EIS profiles can be attributed to changes in the anode impedance. Several other publications also present detailed EIS data concerning the effect of CO on H<sub>2</sub> oxidation at the anode [38–50]. It was demonstrated that the CO poisoning of Pt-containing anodes caused an increase of the total impedance of a cell. The impedance response strongly depended on the exposure time, potential, CO concentration, temperature, and oxygen crossover. An occurrence of a pseudo-inductive loop was detected at low frequency under certain conditions. The loop was observed to be related to the surface relaxation of the anode. Furthermore, the effect of CO on the electrochemical behavior of the fuel cell can be interpreted using the Faraday impedance in addition to the potential-dependent hindrance of the charge transfer [36,38–40,43,46,51–53]. Progressive poisoning with CO of a fuel cell during EIS measurements can complicate the analysis of the data because the examined system should be at steady-state when EIS is running. However, violation of steady-state conditions often occurred, and to solve these problems, time-resolved EIS (TREIS) was introduced [54].

The use of H<sub>2</sub> fuel containing low levels of CO is likely to cause a varying distribution of Pt sites occupied by CO, thus creating areas with low performance located mainly at the inlet of the cell, leading to the redistribution of local/spatial currents and affecting the spatial impedance responses. Therefore, EIS of the cell under CO exposure depends not only on the time of exposure but also on the location inside the membrane electrode assembly (MEA). The evaluation of fuel cell performance with a single cell approach only provides an average of the local voltage, current, and impedance values and does not reveal the spatial behavior of the cell. A segmented cell system is a powerful tool for understanding the details of locally resolved fuel cell processes [55]. There are many examples of segmented cell research applications in PEMFC

studies, including basic investigations of local current distributions [56–60], gas and water management effects [61–65], stack and single cell diagnostic techniques [66–69], defect detection and localization methods [70–74], recirculation [75], start-up, and starvation impact [76–79]. However, there are only a few papers devoted to using segmented cells with poisoned electrodes [16,17,22,30,80]. The authors of these publications discussed the redistribution of the local currents under CO poisoning at relatively high concentrations on the order of 50 ppm up to 3%. Our previous paper [6] presented results concerning the effect of low concentration CO (2 ppm) on PEMFC spatial performance under galvanostatic conditions (0.8 A cm<sup>−2</sup>) and H<sub>2</sub>/H<sub>2</sub>, H<sub>2</sub>/air and H<sub>2</sub>/O<sub>2</sub> gas configurations for the anode/cathode. In that paper, spatial EIS data presented the dynamic responses of the segments upon CO exposure and revealed pseudo-inductance at low frequency and an increase not only in the anode charge transfer resistance but also in the cathode charge transfer resistance. This paper is a continuation of our studies and focuses on detailed spatial EIS characterization of PEMFCs during low CO concentration exposure (2 ppm). The selected CO concentration is still 1 order of magnitude higher than current H<sub>2</sub> fuel cell commodity gas specifications, but in comparison to other studies mentioned is quite low and for the purposes of this analysis may be considered to more closely represent the real operating conditions for PEMFCs. Moreover, a mathematical model describing the temporal evolution of the spatial current densities was adapted and expanded; results are presented and discussed to help further interpretation of the experimental observations.

## 2. Experimental

All the experiments were conducted on a single cell test station using Hawaii Natural Energy Institute's (HNEI) segmented cell system, which enables the simultaneous acquisition of spatially distributed data [68]. The segmented cell approach for this study builds upon the works of Cleghorn et al. [56], the German Aerospace Centre, Stuttgart [81], Ballard Power Systems Inc. [57], and Los Alamos National Laboratory (LANL) [82]. HNEI's segmented cell system is partially based on the LANL design using closed loop Hall sensors and an improved data acquisition system. These enhancements allow the system to perform simultaneous rather than sequential measurements of spatial EIS, spatial linear sweep voltammetry (LSV), and cyclic voltammetry (CV). The segmented cell hardware is based on the HNEI 100 cm<sup>2</sup> cell design. The hardware contains a segmented anode flow field consisting of ten consecutive segments disposed along the path of a ten-channel serpentine flow field. Each segment has an area of 7.6 cm<sup>2</sup>, with its own distinct current collector. The same channel designs are used for both the segmented anode and the standard cathode flow fields (the reactant streams were arranged in a co-flow configuration).

The segmented cell system consists of the cell hardware, the current transducer system, the data acquisition device and a single cell test station. The current transducer system was custom designed. A closed loop Hall sensor (Honeywell CSNN 191) is employed for current sensing. For EIS measurements these sensors show very little inductance over the entire frequency range of interest. The system allows the investigation of as many as 10 current channels in a high (standard) current mode and 16 channels in a low current mode. The standard current mode enables the measurement of segment currents up to 15 A. The current limit of the data acquisition system can be extended to 30 A or more using a unique counter current technology that allows a flexible segmented cell design, high current operation and increased accuracy during EIS experiments. The low current mode of the system yields current measurement up to 375 mA, with an accuracy of  $\pm 2.5\%$ , which is a

convenient feature for CV or LSV experiments. Voltage and current signal data collection was performed with a National Instrument PXI data acquisition instrument operating on HNEI-developed LabView programs.

The cell hardware was operated with standard 100 cm<sup>2</sup> Ion Power MEAs. The anode and cathode electrodes were composed of a 50% Pt/C catalyst coated on a DuPont Nafion 212 membrane with a loading of 0.4 mg<sub>Pt</sub> cm<sup>-2</sup>. We used a Pt/C catalyst as the model system in this work because it exhibits a noticeable response even at low CO poisoning concentrations. The gasket material was made of Teflon, with thicknesses of 203 μm and 178 μm for the anode and cathode, respectively. Sigracet 25 BC was used as the anode and cathode GDLs. The anode used a segmented GDL and gasket configuration, whereas a single GDL was applied at the cathode and an active area of MEA was 76 cm<sup>2</sup>.

During CO exposure, the dry contaminant gas was injected into the humidified feed stream of the anode, keeping the humidification of the gas constant by increasing the temperature setting of the humidifier unit. The anode/cathode testing conditions for the contamination experiments were H<sub>2</sub>/air (or O<sub>2</sub>, or H<sub>2</sub>), 48.3/48.3 kPa<sub>g</sub> backpressure, 100/50% relative humidity and 2/2 stoichiometry. The cell temperature was 60 °C. The cell was operated at a current density of 0.8 A cm<sup>-2</sup> (based on the 76 cm<sup>2</sup> of the active MEA area). The contaminant experiment was divided into three phases:

- Phase 1 was a pre-poisoning period conducted with neat H<sub>2</sub>. The minimum length of Phase 1 was approximately 1/3 of the length of the entire experiment.
- Phase 2 was a poisoning period conducted with a constant amount of contaminant injected into the anode feed stream.
- Phase 3 was a recovery period conducted again with neat H<sub>2</sub>.

The contamination experiment was conducted in H<sub>2</sub>/air, H<sub>2</sub>/O<sub>2</sub> and in a driven H<sub>2</sub>/H<sub>2</sub> mode. For the H<sub>2</sub>/H<sub>2</sub> test, the gas flow rate was 0.847 l min<sup>-1</sup> and the relative humidity was 100% for both the anode and cathode.

The polarization curves (VI curves) in the H<sub>2</sub>/air gas configuration were measured under the same conditions as the contamination experiment. VI curve measurements were also performed in the H<sub>2</sub>/O<sub>2</sub> configuration. In the latter case, the same flow rates were used as in the H<sub>2</sub>/air configuration to keep the water transport in and out of the cell identical at a given total cell current density. Consequently, the stoichiometry for O<sub>2</sub> increased to 9.5. The resulting two different VI curves (H<sub>2</sub>/air and H<sub>2</sub>/O<sub>2</sub>) were used for the determination of a segment's activation, ohmic and mass transfer overpotentials, as described previously [68].

The VI curve measurements and contamination experiments were combined with EIS to determine the cell's and segments' high-frequency resistances (HFR) and to measure the electrochemical impedance spectra for all ten segments and the overall cell. The selected frequency range for the EIS experiments was 0.05 Hz–10 kHz (some measurements were performed in the frequency range of 0.01 Hz–10 kHz), and the amplitude of the sinusoidal current signal perturbation was 2 A, which resulted in a cell voltage response of 10 mV or lower. The HFR was determined from the intercept of the EIS with the x-axis at higher frequencies. The resulting impedance spectra were analyzed based on the fitting of an equivalent electrical circuit (EEC) model. The values of the circuit elements were determined by fitting the experimental data using ZView software (Scribner Associates) at 0.05 Hz to 10 kHz.

CV experiments were conducted for the determination of the electrochemically active surface area (ECA) using a Parstat 2273 potentiostat/galvanostat from Princeton Applied Research. CVs were performed at a cell temperature of 35 °C with a scan rate of

20 mV s<sup>-1</sup>, while 100% humidified hydrogen and nitrogen were supplied to the reference/counter and working electrodes, respectively, at a flow rate of 0.750 l min<sup>-1</sup>. For each measurement, three cycles were applied over a potential range from -0.015–1.1 V vs. the hydrogen reference electrode (HRE). The hydrogen desorption peak area of the third cycle was used to determine the ECA. Hydrogen crossover experiments were performed at the same temperature and flow conditions as the ECA experiments using a single potential sweep from 0.1 to 0.4 V vs. the HRE at a scan rate of 0.1 mV s<sup>-1</sup>.

Before the CO exposure experiment, the segmented cell was assembled using established procedures, conditioned, and subjected to a set of beginning diagnostic tests. The diagnostics consisted of CV to determine the ECAs of the electrodes, LSV to determine the hydrogen crossover current of the cell, and measuring of VI curves with spatial EIS using the H<sub>2</sub>/air and H<sub>2</sub>/O<sub>2</sub> gas configurations to determine the performance, overpotential distributions of the cell, and impedance responses. The same set of diagnostic tests was repeated after the CO experiment. A comparison of the results before and after the CO exposure provided insight into the effects of the contaminant on the spatial properties of the cell. The same MEA sample was used for three CO exposure tests performed at different gas configurations: H<sub>2</sub>/O<sub>2</sub>, H<sub>2</sub>/air and H<sub>2</sub>/H<sub>2</sub>. The MEA was reconditioned after each test.

### 3. Modeling of CO poisoning

#### 3.1. Equivalent electric circuits models for analysis of obtained EIS data

EECs which have been found suitable for fitting EIS data without CO poisoning are presented in Fig. 1. The EECs have several main parts:

- 1)  $R_s$  denotes the serial resistance, which is a sum of the membrane protonic and electronic/ohmic resistances and represents the high-frequency resistance.
- 2)  $L$  represents the high-frequency cable inductance.
- 3) The anode contribution contains  $R_{ct,a}$  and  $C_{dl,a}$ , which describe the charge-transfer resistance of hydrogen oxidation and the capacitance nature of the anode, respectively.
- 4) The cathode circuit has a resistance ( $R_{ct,c}$ ), which represents the charge transfer of the oxygen reduction. The constant phase element (CPE) represents the double-layer capacitance of the real cathode with the roughness of the catalyst layer and a non-uniform catalyst distribution, and  $W$  represents a finite length Warburg diffusion element.

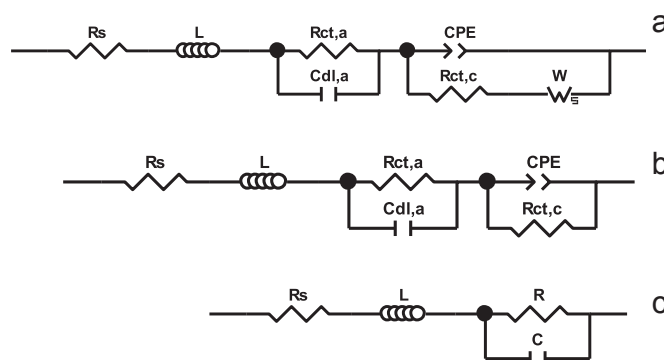


Fig. 1. Equivalent electric circuits for H<sub>2</sub>/air (a), H<sub>2</sub>/O<sub>2</sub> (b) and H<sub>2</sub>/H<sub>2</sub> (c) operating conditions.

The EEC for the cathode electrode operated under air is represented by the well-known Randles cell, which describes the combination of kinetic and diffusion processes in which the capacitance element is replaced by CPE [83–85] (Fig. 1a).

The CPE represents the non-homogeneous distribution of certain physical properties in an electrode, such as the thickness or roughness of the electrode surface that leads to a distribution of time constants in a limited region. The impedance of the CPE was introduced by Cole and Cole [86] and can be written as [87]

$$Z_{\text{CPE}} = \frac{1}{Q_{\text{CPE}}(i\omega)^{p_{\text{CPE}}}} \quad (1)$$

where  $Q_{\text{CPE}}$  is an admittance constant expressed in  $\text{F cm}^{-2}$ ,  $p_{\text{CPE}}$  is an adjustment parameter (whose value belongs to  $[0, 1]$ ,  $i = (-1)^{1/2}$ ), and  $\omega$  is an angular frequency. The  $p_{\text{CPE}}$  factor is related to the depression angle  $\alpha$  by

$$\alpha = (1 - p_{\text{CPE}})90^\circ \quad (2)$$

If  $p$  equals 1, CPE becomes a capacitor:

$$Z_{\text{CPE}} = \frac{1}{Q_{\text{CPE}}i\omega} \quad (3)$$

A CPE with  $p = 0.5$  can be used to produce an infinite length Warburg element:

$$Z_{\text{CPE}} = \frac{1}{Q_{\text{CPE}}\sqrt{i\omega}} \quad (4)$$

A CPE with a  $p$  value of 0 represents resistance:

$$Z_{\text{CPE}} = \frac{1}{Q_{\text{CPE}}} \quad (5)$$

The rate of an electrochemical reaction can be strongly affected by the diffusion of reagents toward the catalyst surface and the removal of products away from the catalyst. Whenever diffusion effects completely dominate the electrochemical reaction mechanism, the impedance is called the Warburg impedance. Impedance of a generalized finite length of a Warburg element can be represented by the following equation [35,88]:

$$Z_W = \frac{R_W \tanh(i\omega T_W)^{p_W}}{(i\omega T_W)^{p_W}} \quad (6)$$

The generalized finite length Warburg element is an extension of another more common element, the finite length Warburg. For the finite length Warburg the parameter  $p_W$  equals 0.5:

$$Z_W = \frac{R_W \tanh\sqrt{i\omega T_W}}{\sqrt{i\omega T_W}} \quad (7)$$

Therefore, the finite length Warburg is characterized by resistance ( $R_W$ ) and the time constant ( $T_W$ ):

$$T_W = \frac{\delta^2}{D} \quad (8)$$

where  $\delta$  is the effective diffusion thickness and  $D$  is the effective diffusion coefficient of the particle.

Using pure  $\text{O}_2$  as the oxidant effectively eliminates the finite length Warburg diffusion element in a cathode circuit (Fig. 1b) and operation under  $\text{H}_2/\text{H}_2$  gas configuration results in the presence of one semicircle, which might be represented by EEC in Fig. 1c.

It was assumed that the shifts in the impedance spectra of PEMFC under CO exposure were mainly caused by changes in the anodic impedance, which is more complicated due to additional reactions involving CO adsorption and oxidation at the electrocatalyst surface. The effects of CO poisoning can be modeled by several EECs, as shown in Fig. 2. The circuits (Fig. 2a, b) represent the impedance data for electrochemical reactions at the anode with a single adsorbed intermediate, where diffusion of the participating species is not rate limiting.

In the circuit at Fig. 2a, the capacitance  $C_1$  is related to the steady-state pseudo-capacitance. The resistance,  $R_1$ , in parallel to  $C_1$ , is associated with the adsorbate formation/removal [37,53,89]. The other resistance,  $R_{\text{ct},a}$ , is known as the charge transfer resistance and relates to the resistance of electron transfer at the anode. Together, these elements describe Faradaic processes at the electrode. In electrochemical cells, the double layer capacitor,  $C_{\text{dl},a}$ , is connected in parallel to the Faradaic impedance of the circuit. Due to the dispersion of capacitance over the electrode a greatly improved fit of the data might be obtained if the double layer capacitor is replaced by a CPE. However, for simplification of EEC model and data fitting a pure capacitance is usually used. The Faradaic impedance can be expressed by

$$Z_F = R_{\text{ct},a} + \left( \frac{1}{R_1} + i\omega C_1 \right)^{-1} \quad (9)$$

The low-frequency inductive loop is often observed in impedance spectra under CO exposure [36,37,43–46]. The loop can be modeled by a pseudo-capacitance in parallel with a resistance similar to Fig. 2a, and negative values of the pseudo-capacitance and resistance represent the inductive behavior [37,41,42,53,89]. A negative capacitance makes no physical sense in electrical terms; however, it can be understood as a decrease in the coverage of adsorbate with potential because

$$C_1 = \frac{dQ}{dE} = q_i \frac{d\theta_{\text{occupied}}}{dE} \quad (10)$$

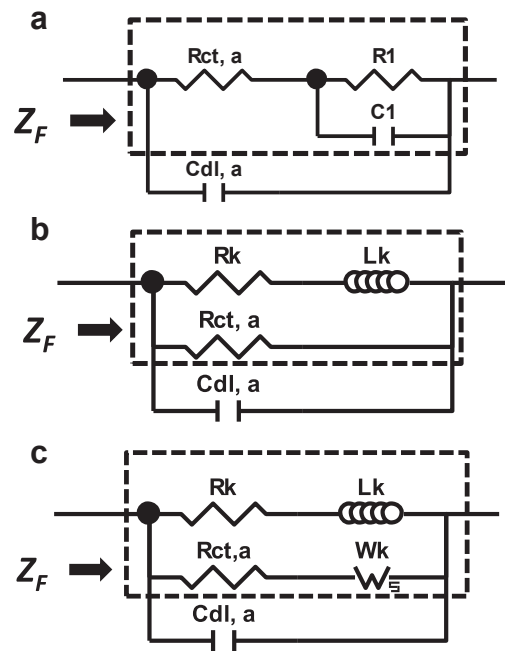


Fig. 2. Equivalent electric circuits for anode impedance under CO poisoning: resistance in parallel to pseudo-capacitance circuit (a), relaxation resistance in series with inductance (b), addition of mass transport limitations to a previous case (c).



where  $q_i$  and  $\theta_{\text{occupied}}$  are the charge density for the monolayer and coverage, respectively. In contrast to a negative  $C_1$ , there is no clear physical meaning of negative resistance  $R_1$ . Negative resistance appears when a current decreases with increasing voltage; additionally, negative resistance is required for a positive time constant ( $\tau = C_1 R_1$ ) [41,53]. Harrington and Conway suggested that the fitting by the inductive circuit (Fig. 2b) is mathematically equivalent to the circuit in Fig. 2a [89]. The inductive circuit is commonly used to represent anode impedance for direct methanol fuel cells [51–53] and PEMFC under CO poisoning [35,46,49]. The inductance  $L_K$  means that the current signal follows a voltage perturbation with a phase delay due to slowness of CO adsorbed coverage relaxation, and  $R_K$  serves to modify the phase-delay. In this case, the Faraday impedance might be expressed by

$$Z_F = \left( \frac{1}{R_{ct,a}} + \frac{1}{R_K + i\omega L_K} \right)^{-1} \quad (11)$$

For a general case, a series combination of  $L_K$  and  $R_K$  defines the relaxation impedance,  $Z_K$ , as it was proposed by Wagner et al. [36,38–40]. Conversion of CO is a potential-dependent process with the rate  $k = k(\varepsilon)$ , which leads to

$$Z_K = \frac{1 + i\omega\tau_K}{I_F \ln k/d\varepsilon} = R_K + i\omega L_K \quad (12)$$

$$R_K = \frac{\Delta\varepsilon}{\Delta I_F} = \frac{1}{I_F \ln k/d\varepsilon} \quad (13)$$

$$X_K = i\omega\tau_K \cdot R_K = i\omega L_K \quad (14)$$

Here,  $I_F$  denotes the Faraday current,  $\tau_K$  is the time constant of relaxation, and  $\ln k/d\varepsilon$  is the first derivative of the reciprocal relaxation time constant ( $k = 1/\tau_K$ ). The relaxation impedance  $Z_K$  can be split into the relaxation resistance ( $R_K$ ) and relaxation inductivity ( $X_K$ ) with pseudo-inductance ( $L_K = \tau_K R_K$ ) [38].

Fig. 2c presents an EEC where diffusion limitations exist. The circuit was suggested for a PEMFC operated under 100 ppm CO exposure and may be expressed as [36,38–40]

$$Z_F = \frac{R_{ct,a} + Z_N}{1 + R_{ct,a}/Z_K} \quad (15)$$

where  $Z_N$  is the Nernst impedance and is equivalent to the finite length Warburg element ( $Z_{Wk}$ ). In our work, the fuel cell operated under 2 ppm of CO, which allows us to assume that there are no diffusion limitations of participating species and that  $Z_{Wk} = 0$ . Based on this assumption and our previous results [6], the anode EEC under CO poisoning presented in Fig. 2b was selected for the evaluation and analysis of EIS, and the final EECs are given in Fig. 3. For  $H_2/H_2$  operation (Fig. 3c), pure capacitance was transformed to CPE because it provided more adequate fitting results.

The complete impedance ( $Z_T$ ) of the cell under CO poisoning is represented by the EECs shown in Fig. 3 and can be grouped as following:

$$Z_T(\omega, t) = Z_S(\omega, t) + Z_{\text{anode}}(\omega, t) + Z_{\text{cathode}}(\omega, t) \quad (16)$$

where  $Z_S(\omega, t)$  is the series impedance presented by  $R_S$  and  $L$ ,  $Z_{\text{anode}}(\omega, t)$  is the anode impedance, and  $Z_{\text{cathode}}(\omega, t)$  is the cathode impedance contribution. Moreover, the total impedance depends on the applied frequency and time of CO exposure because the frequency dependence is related to the EEC dynamics while the time dependence is associated with the fact that the system is not

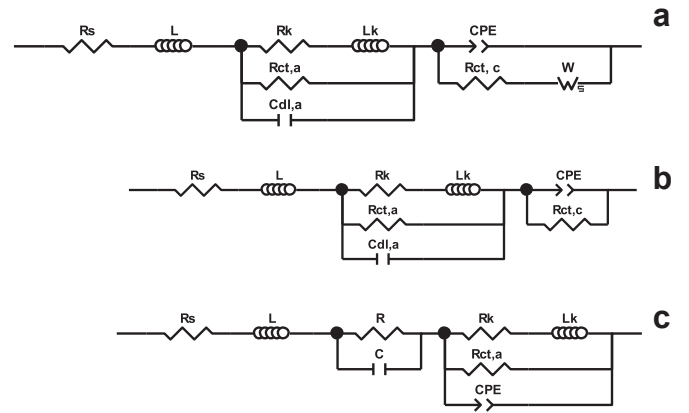


Fig. 3. EEC for EIS data obtained during operation under CO poisoning and various gas configurations:  $H_2 + CO/\text{air}$  (a),  $H_2 + CO/O_2$  (b),  $H_2 + CO/H_2$  (c).

in a steady-state condition and can change impedance during measurement.

The anode impedance in the Laplace domain for air, oxygen or a symmetric cell is described in Eq. (17):

$$Z_{\text{anode}}(i\omega) = \frac{R_K R_{ct,a} + i\omega L_K R_{ct,a}}{(i\omega)^2 C_{dl,a} R_{ct,a} L_K + i\omega (C_{dl,a} R_K R_{ct,a} + L_K) + R_K + R_{ct,a}} \quad (17)$$

The cathode impedance is expressed by Eq. (18), where the impedance of the cathode double layer capacitance (CPE) is described by Eq. (1):

$$Z_{\text{cathode}}(i\omega) = \frac{1}{(i\omega)^{p_{CPE}} Q_{CPE} + (1/(R_{ct,c} + Z_W(i\omega)))} \quad (18)$$

The impedance  $Z_W(i\omega)$  is represented as a second-order function [90]. Eq. (18) can be simplified for pure  $O_2$  operation:

$$Z_{\text{cathode}}(i\omega) = \frac{R_{ct,c}}{(i\omega)^{p_{CPE}} Q_{CPE} R_{ct,c} + 1} \quad (19)$$

The series impedance of the cell can be calculated from the following expression:

$$Z_S(i\omega) = R_S + i\omega L \quad (20)$$

### 3.2. Model for analysis of temporal evolution of current density distribution

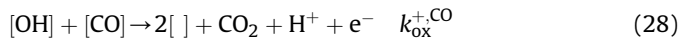
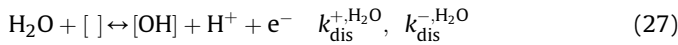
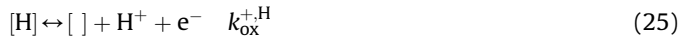
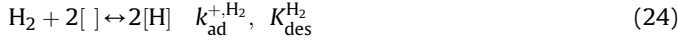
An attempt is made here to apply a simple mathematical model to achieve a qualitative description of the observed current density distributions under CO exposure. During the CO poisoning, the overall voltage and currents do not depend on the frequency response of the EECs. In a pseudo-steady state, the impedances depend only on resistances due to the great values of the time constants. Therefore, the complete impedances can be presented as follows:

$$Z_T^{\text{air}}(t) = R_S(t) + R_{ct,c}(t) + R_W(t) + \frac{R_K(t) R_{ct,a}(t)}{R_K(t) + R_{ct,a}(t)} \quad (21)$$

$$Z_T^{O_2}(t) = R_S(t) + R_{ct,c}(t) + \frac{R_K(t) R_{ct,a}(t)}{R_K(t) + R_{ct,a}(t)} \quad (22)$$

$$Z_T^{H_2}(t) = R_S(t) + R(t) + \frac{R_K(t)R_{ct,a}(t)}{R_K(t) + R_{ct,a}(t)} \quad (23)$$

The dynamic response of the segment resistances (Eqs. (21)–(23)) should be represented by a mechanism that accounts for the following chemical and electrochemical reactions [9,14]:



For this purpose, the CO poisoning model developed in Refs. [14,91,92] was used here and modified to describe the temporal evolution of the spatial current densities. This model considers the surface kinetic reactions at the anode:  $r_T$  is the Tafel reaction (Eq. (29)),  $r_V$  defines the Volmer contribution (Eq. (30)),  $r_{ad}^{CO}$  is the rate of CO adsorption (Eq. (31)),  $r_{dis}^{H_2O}$  is the dissociation of  $H_2O$  (Eq. (32)), and  $r_{ox}^{CO}$  is the CO oxidation rate reaction (Eq. (33)).

$$r_T = k_{ad}^{+,H_2} (p\theta^2 - K_{des}^{H_2}\theta_H^2) \quad (29)$$

$$r_V = 2k_{ox}^{+,H}\theta_H \sinh\left(\frac{\alpha V F \eta_a}{RT}\right) \quad (30)$$

$$r_{ad}^{CO} = k_{ad}^{+,CO} (x_{CO}\theta p - K_{des}^{CO}\theta_{CO}) \quad (31)$$

$$r_{dis}^{H_2O} = k_{dis}^{+,H_2O}\theta e^{\left(\frac{\alpha_{H_2O} F \eta_a}{RT}\right)} - k_{dis}^{-,H_2O}\theta_{OH} e^{\left(\frac{-(1-\alpha_{H_2O}) F \eta_a}{RT}\right)} \quad (32)$$

$$r_{ox}^{CO} = k_{ox}^{+,CO}\theta_{CO}\theta_{OH} e^{\left(\frac{\alpha_{CO} F \eta_a}{RT}\right)} \quad (33)$$

Here,  $k_n^+$  and  $k_n^-$  are the reaction rate constants of the forward and backward  $n$  reaction,  $K_{des}^{H_2}$  and  $K_{des}^{CO}$  are the equilibrium constants for  $H_2$  and CO desorption, respectively. The pressure in the channel is represented by  $p$ .  $T$  is the average temperature.  $R$  and  $F$  are the gas constant and Faraday constant, respectively. The anode overpotential is described by  $\eta_a$ , and the mole fraction of CO is  $x_{CO}$ .

The balance of species coverage is represented by Eq. (34), where the species are CO, OH and H. Vacant surface sites are represented by  $\theta$ .

$$\theta + \theta_{CO} + \theta_{OH} + \theta_H = 1 \quad (34)$$

The coverage dynamics are calculated in Eqs. (35)–(37), and the catalyst sites are described by  $\gamma C_t$ , where  $\gamma$  represents the roughness factor and  $C_t$  is the atom mole density per  $cm^2$ .

$$F\gamma C_t \frac{d\theta_{OH}}{dt} = r_{dis}^{H_2O} - r_{ox}^{CO} \quad (35)$$

$$F\gamma C_t \frac{d\theta_{CO}}{dt} = r_{ad}^{CO} - r_{ch}^{CO} - r_{ox}^{CO} \quad (36)$$

$$F\gamma C_t \frac{d\theta_H}{dt} = r_T - r_V \quad (37)$$

Eq. (36) accounts for the fact that CO may be oxidized via a chemical pathway ( $r_{ch}^{CO}$ ):



Chemical oxidation of CO is controlled by the rate of permeation of  $O_2$  through the membrane, and the oxidation kinetic is rapid. Under steady-state diffusion conditions, the flux of  $O_2$  can be expressed as [29]

$$N_{O_2} = \frac{KDP_{O_2}}{L} \quad (40)$$

$N_{O_2}$  is the steady-state flux of  $O_2$ , which crosses the membrane due to diffusion.  $K$  is the Henry's law constant,  $D$  is the diffusion coefficient of  $O_2$  in the membrane,  $L$  is the thickness of the membrane, and  $P_{O_2}$  is the partial oxygen pressure in the cathode. Furthermore, we used the parameter  $\mu$  to account for the selectivity of  $O_2$  for the oxidation of CO [29]:

$$r_{ch}^{CO} = \mu N_{O_2} \quad (41)$$

Considering the capacitive and faradaic currents and using the equation of charge conservation, the time evolution of the anode potential can be calculated as

$$C_{dl} \frac{d\eta_a}{dt} = \frac{i}{\varepsilon} - F(r_V + r_{ox}^{CO} + r_{dis}^{H_2O}) \quad (42)$$

where  $i$  is the electric current density and  $\varepsilon$  is a fitting parameter related to the active area. The current is the sum of the faradaic current and the capacitive current. The capacitive current is written as the product of the double-layer capacity  $C_{dl}$  and the temporal change of the potential  $\eta_a$ . The faradaic current includes the H and CO electrooxidation currents ( $r_V$  and  $r_{ox}^{CO}$ ) and the net current of water dissociation ( $r_{dis}^{H_2O}$ ) [14,92,93].

To represent the anode channel with a CO flow, a simple straight channel has been modeled as illustrated in Fig. 4. The model of the channel has been discretized into control volumes; each of these control volumes is connected to the electrochemical model described above. The injected CO at the channel inlet is dragged by the anode gas flux. The effect of cross currents in the GDL was not taken into account by the model, since current density

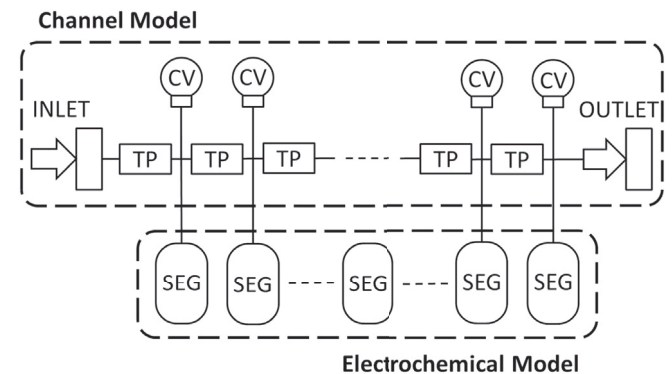


Fig. 4. Model diagram of straight channel. The elements TP and CV describe the transport and balance equations, respectively.

distributions, gradients of CO concentration and pressure drop along flow channel are significantly larger than channel to channel. The concentration of CO is homogeneous and constant in each control volume because well-mixed gas conditions are assumed. The flux of CO in the channel is calculated based on the assumption of pure advection of CO, and  $A_v$  depends on the main flux in the channel, in this case the  $H_2$  flux:

$$\vec{j}_{CO} = A_v x_{CO}^{chan} \quad (43)$$

The discretization of the channel allows us to simulate the distribution of CO along the channel, where the amount of CO flux toward the catalyst surface is  $\vec{j}_{CO}$ . The relationship between  $\vec{j}_{CO}$  and the rate of CO adsorption is represented by the dimensional parameter  $\beta$ :

$$\vec{j}_{CO}^{IN} = \beta r_{ad}^{CO} \quad (44)$$

The total flux of CO is the sum of the CO transported in the channel and the consumption of CO in the anode through the CO adsorption reaction:

$$\vec{j}_{CO} = C_v \frac{dx_{CO}^{chan}}{dt} + \vec{j}_{CO}^{IN} \quad (45)$$

where the capacity related to the discretized volume is represented by  $C_v$ .

The electric current produced in each segment,  $i_j$ , is calculated from the following expression:

$$i_j = (V_{OC} - \eta_a) R_{segment} \theta_H \quad (46)$$

$$i_{cell} = \sum_{j=1}^{10} i_j \quad (47)$$

where  $V_{OC}$  is the open circuit voltage of the cell, and the impedance of the segment in steady-state,  $R_{segment}$ , is a free variable. Eq. (46) is a simple polarization curve around a set point  $R_{segment}$ , where the main overpotential is caused by anode processes. The set point,  $R_{segment}$ , is a simplified approach to resistance described in Eqs. (21)–(23) depending on the operating cathode gas configuration. Eq. (47) relates to the total applied current,  $i_{cell}$ , as a sum of local currents,  $i_j$ .

The model described above of a fuel cell channel operated under  $H_2 + CO/O_2$  conditions was simulated using the Modelica language and Dymola. For reducing the complexity of the model, which primarily focuses on the anode poisoning processes, diffusion and flooding were not implemented, and the current densities of all the segments are equal in the pre-poisoning and recovery stages. The parameters used in the simulation are listed in Table 1 and were acquired from the literature [14,29,91–94], with the exception of the values that were not available, which were fitted to reproduce the experimental data.

## 4. Results and discussion

### 4.1. Effect of CO injection during $H_2/O_2$ operation

All the experiments were performed under galvanostatic mode with an overall constant current density of  $0.8 \text{ A cm}^{-2}$ . Fig. 5 presents profiles of the segment voltages and current densities normalized to its initial values vs. experiment time. The pre-poisoning period was performed with neat  $H_2/O_2$  for 70 h. The segment voltages and the overall cell voltage were 0.665 V due to

**Table 1**

Values of model parameters used in the simulation.

Parameter	Description	Value
$A_v$	Advection gas flux	$1 \text{ l min}^{-1}$
$C_{dl}$	Double layer capacitance	$0.450 \text{ F}$
$C_r$	Catalyst sites factor	$2.2 \times 10^{-9} \text{ mol cm}^{-2}$
$C_v$	Gas capacitance	$2 \text{ l}$
$D$	Diffusion coefficient of $O_2$ in membrane	$1.7 \times 10^{-6} \text{ cm}^2 \text{ s}^{-1}$
$F$	Faraday's constant	$96485.3415 \text{ C mol}^{-1}$
$K$	Henry's law constant	$8.86 \times 10^{-7} \text{ mol cm}^{-3} \text{ atm}^{-1}$
$k_{ad}^{+H_2}$	Constant of forward reaction rate of $H_2$ adsorption	$402 \text{ A cm}^{-2} \text{ atm}$
$K_{des}^{H_2}$	Equilibrium constant for $H_2$ desorption	$0.5 \text{ atm}$
$k_{ad}^{+CO}$	Constant of forward reaction rate of CO adsorption	$50 \text{ A cm}^{-2} \text{ atm}$
$K_{des}^{CO}$	Equilibrium constant for CO desorption	$1.5 \times 10^{-6} \text{ atm}$
$k_{ox}^{+CO}$	Constant of forward reaction rate of CO oxidation	$0.13 \text{ A cm}^{-2}$
$k_{dis}^{+H_2O}$	Constant of forward reaction rate of $H_2O$ dissociation	$1.2 \times 10^{-3} \text{ A cm}^{-2}$
$k_{dis}^{-H_2O}$	Constant of backward reaction rate of $H_2O$ dissociation	$2760 \text{ A cm}^{-2}$
$k_{ox}^{+H}$	Constant of forward reaction rate of $H_2$ oxidation	$4 \text{ A cm}^{-2}$
$L$	Membrane thickness	$5 \times 10^{-3} \text{ cm}$
$p$	Gas pressure	$1.48 \text{ atm}$
$P_{O_2}$	Partial pressure of $O_2$ in the cathode	$1.48 \text{ atm}$
$R$	Ideal gas constant	$8.314472 \text{ J mol}^{-1} \text{ K}^{-1}$
$T$	Temperature	$333 \text{ K}$
$V_{OC}$	Open circuit voltage	$1 \text{ V}$
$x_{CO}^{IN}$	Inlet CO concentration	$2 \times 10^{-6} \text{ mol CO mol H}_2^{-1}$
$\alpha_v$	Transfer coefficient for $H_2$	$0.5$
$\alpha_{CO}$	Transfer coefficient for CO	$0.5$
$\alpha_{H_2O}$	Transfer coefficient for $H_2O$	$0.5$
$\beta$	Dimensional parameter	$5 \times 10^{-3} \text{ l s min}^{-1} \text{ mol}^{-1}$
$\gamma$	Roughness factor	$300$
$\varepsilon$	Fitting parameter	$4$
$\mu$	$O_2$ selectivity	$3 \times 10^3$

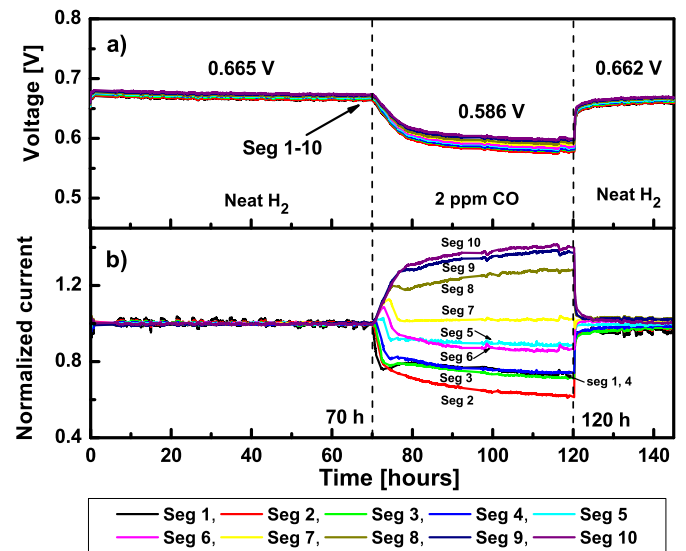


**Fig. 5.** Voltage (a) and normalized current densities (b) of individual segments vs. time for an overall current density of  $0.8 \text{ A cm}^{-2}$  and 2 ppm CO. Anode/cathode:  $H_2/O_2$ ,  $0.847/2.018 \text{ l min}^{-1}$ , 100/50% RH, 48.3/48.3 kPa<sub>g</sub>, 60 °C.

the design of the segmented cell system and small size of the segmented electrodes and cell. The performances of individual segments were constant and did not change with time in the pre-poisoning phase. After the injection of 2 ppm CO into the hydrogen stream, a fast decrease of the segments' voltages occurred and current density redistribution was observed. The transition period to reach steady state lasted approximately 10 h. At steady state, the segments voltages settled at 0.586 V, which yielded a performance loss of 0.089 V. Under CO exposure, the inlet segments 1–4 exhibited the lowest current density magnitudes, while the outlet segments 8–10 showed an increase in current density. A decrease of the inlet segments' performance up to 60% of their initial performance occurred due to adsorption of CO mainly at the inlet part of the cell, which resulted in a decrease of the CO concentration downstream and kept the catalyst layer effectively unpoisoned at the outlet of the cell. Moreover, operation of the cell in galvanostatic mode required obtaining a constant current out of the entire cell and because the current of the inlet segments decreased after CO injection an increase as high as 40% in the current of segments 9 and 10 occurred. A similar current density distribution under galvanostatic mode was previously reported in other papers [16,22,30]; in addition, a comparable close cooperative behavior of Pt microelectrodes during CO electro-oxidation was presented in Ref. [95]. After switching the fuel from the  $H_2 + 2$  ppm CO mixture to pure  $H_2$ , the cell and segments recovered their performances very close to the initial voltage values of 0.662 V (vs. 0.665 V) within 1 h.

To support the observed experimental trend in the current redistribution, a simulation of the current density was performed using the models described in Section 3.2. Fig. 6a presents the simulation results of the spatial current density evolution with the assumption that Eqs. (24)–(28), (38), (39) represent the chemistry

of the processes at the anode and that oxidation of CO occurs through electrochemical and chemical pathways. For simplification purposes, the diffusion and flooding processes were not considered in the model and the current density of all segments are equal in the pre-poisoning and the recovery stages. The segments with lower currents were located in the inlet, while the outlet exhibited the greater performance. The dynamic behavior of current density at the beginning of CO injection was in good agreement with the experimental data. The main difference between the experimental and simulated data is in the dynamics at the recovery stage. The experiments showed a first order decay, while the simulations revealed overshoots due to a higher order dynamics (Figs. 5 and 6a). Time for reaching the steady state at the recovery stage is close (~4 h) in simulations and the real test. Moreover, the model predicts a local CO concentration distribution at steady-state (Fig. 6b). A significant decrease of the CO concentration is observed for segments 7–10. A comparison of the simulated and experimental results reveals that the proposed model adequately represents the behavior of the fuel cell under CO exposure and might be used for prediction purposes in the future.

Fig. 7 presents the experimental impedance data and EEC modeling results for all ten segments and the overall cell recorded at different phases of the experiment. The EIS curve of the fuel cell operated without CO poisoning consists of several semicircles: a high-frequency anode arc (usually, it is negligible; however, it might be observed for low current operation), a high-frequency cathode arc attributed to a charge transfer resistance and double layer capacitance of oxygen reduction reaction, and a low-frequency arc presenting mass transport limitations within the electrode [32]. Operation with pure  $O_2$  as an oxidant eliminated mass transport obstacles at the cathode and simplifies the impedance spectrum, leaving a small high-frequency anode and significant high-frequency cathode arcs, reflecting the charge transfer processes at the electrodes. These curves produced during the prepoisoning phase were modeled using EEC in Fig. 1b, which provided adequate fitting to the EIS data.

After 1 h of CO injection, there was a slight increase in the impedance of segments 1–3, while the other segments did not show any changes. Moreover, for these segments, a drift of the impedance values was observed at low frequency, indicating changes in the segments' behavior during the measurement because recording EIS at low frequency required a finite time [54]. Thus, we excluded the low-frequency part of the curves from the EEC fitting. Segments 1–5 exhibited an increase of the impedance response after 3 h of CO exposure. Poisoning within 5 h resulted in EIS changes for segments 1–7. Segment 8 revealed only a slight increase in EIS after 49 h, while segments 9 and 10 were not affected by CO. Such a negligible impact of CO on the outlet segments might be explained by a low CO concentration in the  $H_2$  stream (Fig. 6b), strong adsorption of CO on Pt at the inlet part of the cell, and operation with pure  $O_2$ . Moreover, a typical pseudo-inductive loop for  $H_2 + CO$  operation was not obtained in the low-frequency region. EEC presented in Fig. 3b was used for fitting the EIS data under CO exposure. However, a lack of pseudo-inductive behavior allowed us to simplify the circuit to the one depicted in Fig. 1b. The EIS curves after 1 h of recovery revealed significant decreases in the segments' impedances. Total recovery was observed after ~4–5 h of operation at pure  $H_2$ .

High-frequency region (10 kHz–5 kHz) for individual segments was represented by pure inductance most likely due to load connection wire setup [96]. However, EIS curves for the total cell demonstrated high-frequency loop, which was close to capacitive behavior [97–100]. This behavior might be attributed to structural properties of MEAs, hardware size, measurement setup and cabling [96–98]. High-frequency region is not associated with the

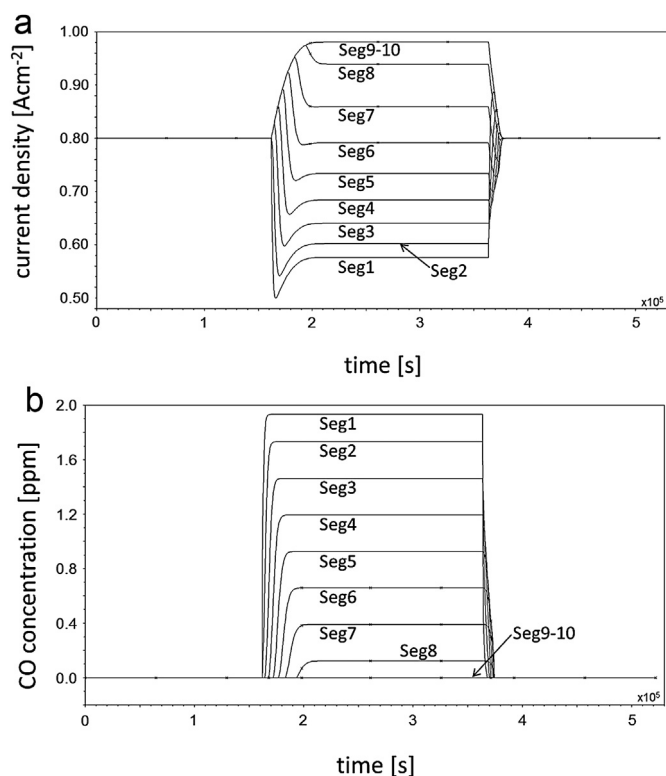
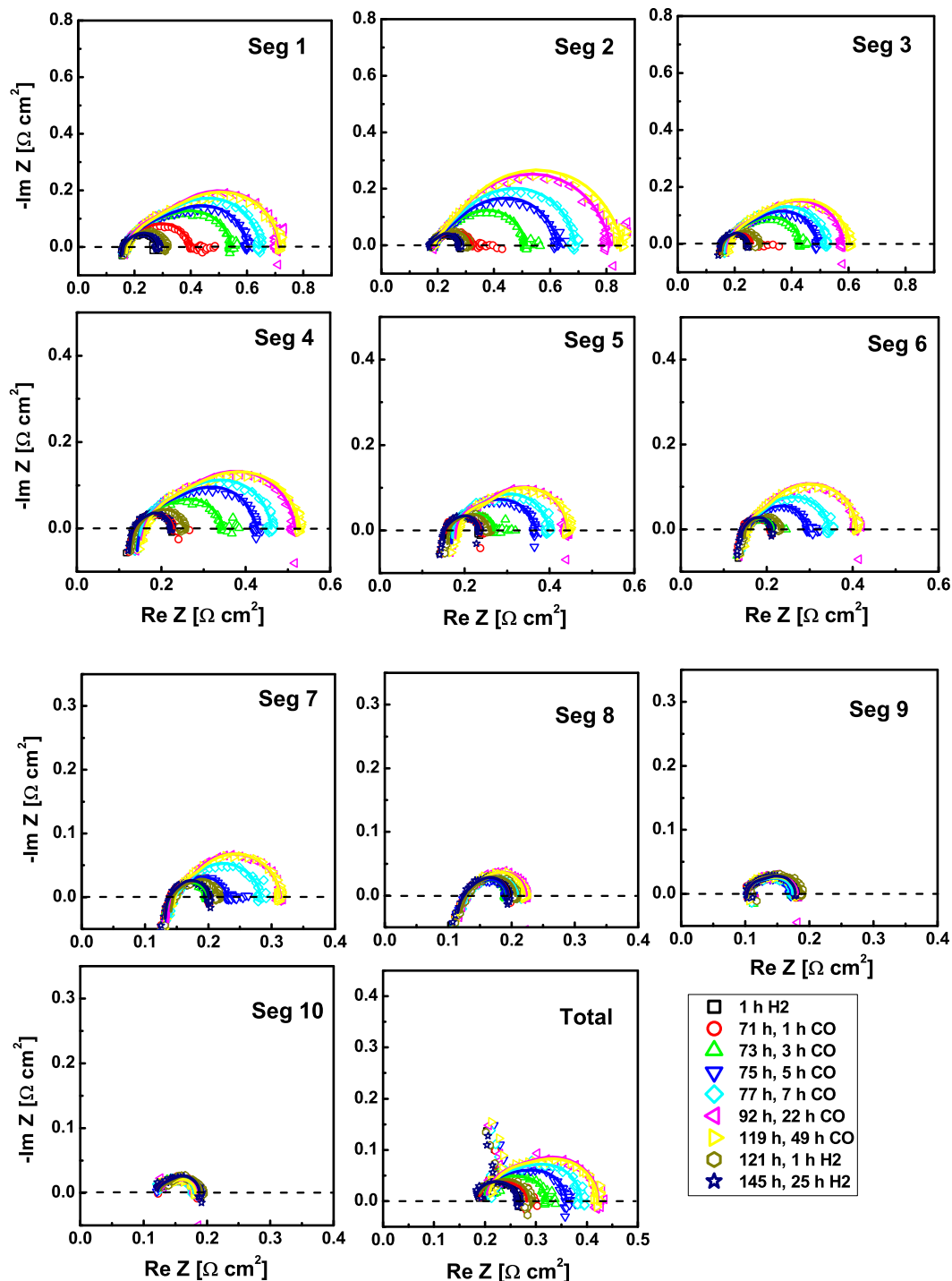


Fig. 6. Simulation of current (a) and CO concentration (b) distributions in galvanostatic mode under  $H_2/O_2$  operating conditions. The parameters used in the simulation are listed in Table 1.

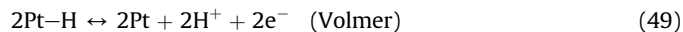




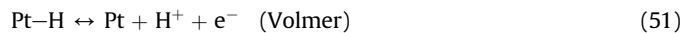
**Fig. 7.** EIS for segments 1–10 and the overall cell during 2 ppm CO exposure test at  $0.8 \text{ A cm}^{-2}$ . The experimental data are presented by symbols, and the modeling results are represented by solid lines. Anode/cathode:  $\text{H}_2/\text{O}_2$ ,  $0.847/2.018 \text{ l min}^{-1}$ , 100/50% RH, 48.3/48.3 kPa<sub>g</sub>, 60 °C. The spectrum at 92 h was recorded up to 0.01 Hz; the others were recorded up to 0.05 Hz.

electrode processes and the impedance response of the overall cell exhibited the same trend as the inlet segments.

To understand the behavior of PEMFC in the presence of CO, the mechanism of the CO and  $\text{H}_2$  reactions should be considered. The oxidation of hydrogen on Pt was shown to proceed according to the Tafel–Volmer mechanism, where the hydrogen dissociation reaction is the rate-controlling step [101]:

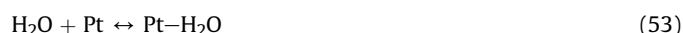


Another mechanism proposed for hydrogen oxidation reaction (HOR) is the Volmer–Heyrovsky sequence [101]:



Oxidation of hydrogen on Pt occurs in the range of 0–0.2 V. Moreover, Eqs. (48)–(51) indicate that the reaction is sensitive to the surface coverage (Pt–H) and that a decrease of available Pt sites results in changes of the reaction rate. Moreover, the rate-determining step depends on the CO coverage. For  $\theta_{\text{CO}} < 0.6$ , the hydrogen oxidation reaction occurs via the Tafel–Volmer mechanism with the Tafel reaction as the rate-determining step at the low CO coverage, while the Volmer step controls the overall reaction rate at the medium CO coverage. When the CO coverage is higher than 0.6, the Heyrovsky–Volmer mechanism is operative for the HOR with Heyrovsky sequence as the rate-determining step [102].

Oxidation of CO to CO<sub>2</sub> can occur via chemical and/or electrochemical pathways. The electrochemical mechanism involves a reaction between adsorbed CO and oxygen-containing species, the nature of which remains under discussion. This species may be adsorbed H<sub>2</sub>O molecules or hydroxyl (–OH) species [103–105]. The ignition potential of the CO oxidation on Pt at 60 °C is in the range of 0.4–0.5 V, and full electrochemical oxidation occurs at 0.6–0.9 V [8,27,106,107].



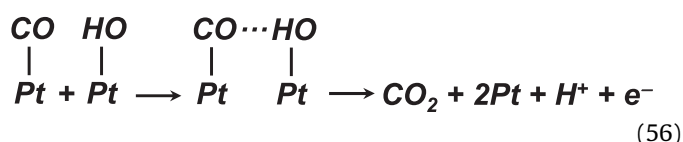
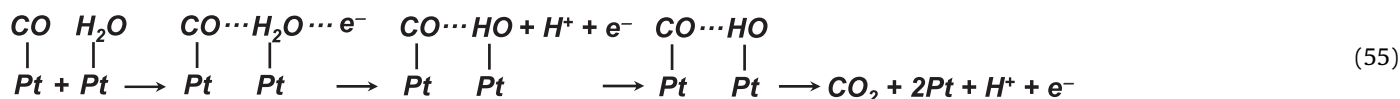
contributions of CO poisoning, the “geometrical blocking” or “electronic factor”; these factors should be considered together.

Chemical oxidation of CO should also be considered due to the diffusion of oxygen from the cathode to the anode compartment. It is well known fact that bleeding a small amount of oxygen or air into the anode gas stream is very effective in mitigating CO poisoning [4,13,21–25]. CO is oxidized by oxygen via a non-electrochemical surface redox mechanism, which is similar to the preferential oxidation process [29]:



The anode overpotential caused by the presence of CO in this case equals 0.085 V, which is significantly low for the electrochemical oxidation of CO. Moreover, no low-frequency inductive loop is present in EIS, which usually indicates a slow electrochemical process involving a single adsorbed intermediate formation/removal at an electrode. These reasons allow us to assume that the chemical mechanism is dominant, as demonstrated in our previous paper [6].

The analysis of EEC modeling of EIS data was performed using serial resistance ( $R_s$ ), anode ( $R_{\text{ct,a}}$ ) and cathode charge transfer ( $R_{\text{ct,c}}$ ) resistances. Fig. 8 shows the distributions of these parameters



Thus, CO more strongly chemisorbs on the platinum sites than hydrogen, as indicated by the greater potential required for the CO oxidation, and even a small concentration of CO can cover the entire catalyst surface. However, the rate of hydrogen oxidation on the few remaining platinum sites is rapid so it controls the surface potential [8]. Unfortunately, this potential remains less than the potential needed to oxidize CO; thus, the CO coverage remains, which is dictated by the CO adsorption isotherm (Temkin isotherm) [108]. The adsorbed CO blocks sites for dissociative chemisorption of hydrogen, which reduces the current because the hydrogen chemisorption is assumed to be second order in the vacant sites coverage ( $\theta = 1 - \theta_{\text{CO}} - \theta_{\text{H}} - \theta_{\text{OH}}$ ). The coverage of CO is a function of the potential as well as the CO partial pressure. In addition, CO and H<sub>2</sub> do not interact during their co-adsorption at temperatures of less than 200 °C. However, it was noted that the apparent activation energy for hydrogen oxidation increases in the presence of CO [109]. It is very difficult experimentally to separate the two main

as functions of the segment positions at different stages of the test. Under CO exposure, segments 1–7 exhibited an increase in the serial resistance, anode and cathode charge transfer resistances. In addition, segments 8–10 did not show any changes in EIS. An increase in HFR for the inlet segments might be due to the local current redistribution, changes in water production and local water management, which can lead to insufficient membrane hydration. As mentioned previously, the CO poisoning of the Pt anode resulted in an increase of the apparent activation energy of hydrogen oxidation and blocking of the Pt surface; thus, these geometrical and electronic effects were reflected by an increase of the anode charge transfer resistance. The effective charge transfer resistance was affected by the concentrations of the charged and uncharged species (H<sub>2</sub>O). The poisoning of the anode caused a local inhomogeneous distribution of the generated H<sup>+</sup> and a resulting inhomogeneous distribution of the protonated and associated water molecules at the anode electrode and membrane. This process created an uneven distribution of these species at the cathode, which led to an increase in the cathode charge transfer resistance [40]. On the other hand, CO poisoning resulted in a 40–60% decrease in the current for the segments 1–6 (Fig. 5). Spatial EIS recorded for these segments corresponded to a lower current compared with the pre-poisoning stage. At lower current densities, the cathode charge transfer resistance was larger. The EIS and EEC data revealed progressive CO poisoning downstream as well as a dynamic character of the poisoning with the time of the exposure. It is clear that the segments achieved a steady-state after 7–10 h of CO injection. The EIS curves after 1 h of recovery showed significant decreases in the segment impedance responses, and full recovery was observed after ~4–5 h of stopping the CO injection.

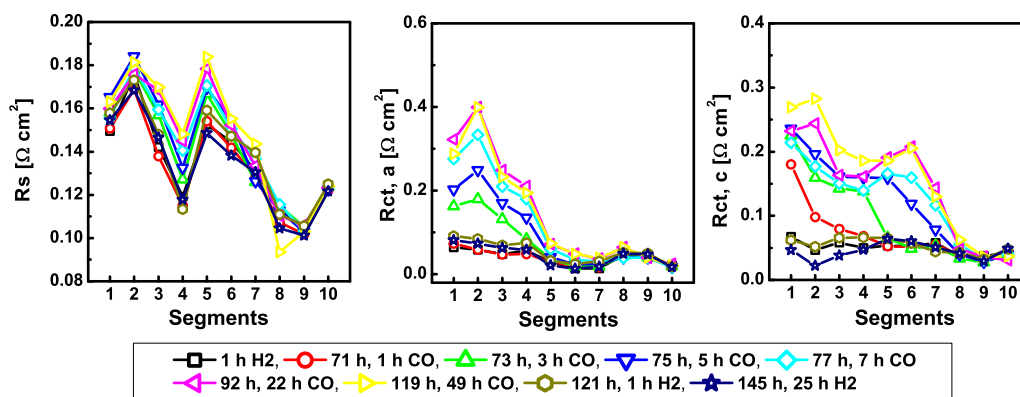


Fig. 8. Distributions of serial resistance ( $R_s$ ), anode ( $R_{ct,a}$ ) and cathode ( $R_{ct,c}$ ) charge transfer resistances at various CO exposure times and  $H_2/O_2$  operation. EEC fitting was performed in the frequency range of 10 000–0.05 Hz.

#### 4.2. Effect of CO injection during $H_2/H_2$ operation

To study the hydrogen oxidation reaction (HOR) with CO poisoning, we performed the same experiment as for the  $H_2/H_2$  gas configuration.  $H_2$  was fed into the cathode, which served as a “pseudo” reference electrode. The hydrogen for the anode and cathode was fully humidified and supplied at a constant flow rate of  $0.847 \text{ l min}^{-1}$ .

The voltage responses and normalized current densities as a function of the test time for all the segments for driven  $H_2/H_2$  operation are presented in Fig. 9. During the pre-poisoning phase, the segments' voltages were 0.130 V. For pure hydrogen operation, the range of individual segment current densities measured was  $0.67\text{--}0.88 \text{ A cm}^{-2}$ . After CO injection, the anode potential increased to 0.425 V, resulting in a voltage difference of  $\sim 0.295 \text{ V}$ . The current density behavior was similar to the previous case with  $H_2/O_2$ . The injection of 2 ppm CO resulted in a decrease in the current densities of the inlet segments ( $0.51 \text{ A cm}^{-2}$  for segment 1) and an increase for the outlet segments ( $1.16 \text{ A cm}^{-2}$  for segment 10). The outlet segments had to increase their currents to maintain the same overall current density of  $0.8 \text{ A cm}^{-2}$ . The cell and segments recovered their performances almost to their initial values of

0.140 V (vs. 0.130 V) within 1 h after stopping CO injection. The observed difference in the cell voltage before and after the CO test ( $\sim 10 \text{ mV}$ ) might be due to the lack of oxygen crossover and chemical oxidation of carbon monoxide at the anode.

The results of the impedance measurements and EEC fitting are presented in Figs. 10 and 11. It should be noted that at  $H_2/H_2$  operation, EIS revealed a small semicircle, which was most likely a combination of two arcs. The arc in the high-frequency region can be attributed to the process involving oxidation of the adsorbed hydrogen atoms according to Eq. (49), while the arc in the low-frequency region is assigned to the dissociative adsorption of hydrogen (Eq. (48)) [31]. Alternatively, the low-frequency arc could be associated with the slow mass transfer processes; however, the effect of a limited gas supply was avoided in the work by applying pure hydrogen with a high flow rate. As mentioned in Ref. [8], slow dissociation of adsorbed hydrogen molecules is the rate-limiting stage for the oxidation of hydrogen. Thus, the EEC for fitting the  $H_2/H_2$  impedance response has only one circuit (Fig. 1c).

CO exposure within 1 h led to an increase of the impedances of segments 1–3. Additionally, for these segments, a drift of the impedance values was observed at low frequency, indicating changes in the segments during the measurement. This feature is similar to that observed during  $H_2/O_2$  operation. Injection of CO within 5 h resulted in a significant increase of impedance for segments 1–5 and a slight growth for segments 6–9. The segments reached steady-state after 7 h of CO exposure. The impedance spectra of segments 1–8 had a negligible high-frequency arc and significant semicircle, corresponding to the processes at the anode:  $H_2$  oxidation in the presence of CO and processes involving CO conversion. The impedance curves after 7 h of CO exposure were recorded up to 0.05 Hz, which allowed us to observe a pseudo-inductive loop for segments 1–4. The impedance behavior under these operating conditions can be described by the EEC depicted in Fig. 3c, where the CO poisoning affects oxidation of the adsorbed hydrogen atoms (Eq. (49)). Segments 9 and 10 revealed more complicated impedance spectra, most likely due to the effect of water accumulation at the outlet part of the cell, and they were excluded from EEC fitting. The curves presenting EIS after 25 and 47 h of CO injection were measured in the frequency range of 0.01 Hz–10 kHz. The diameters of these curves were close to those of the previous time point; however, the presence of the pseudo-inductive loop became clear for segments 1–6. Segments 7 and 8 did not exhibit any inductive behavior at low frequency. It should be noted that the EIS curves recovered after changing from the  $H_2 + 2 \text{ ppm CO}$  mixture to pure  $H_2$ , as did the segments' voltages and current densities.

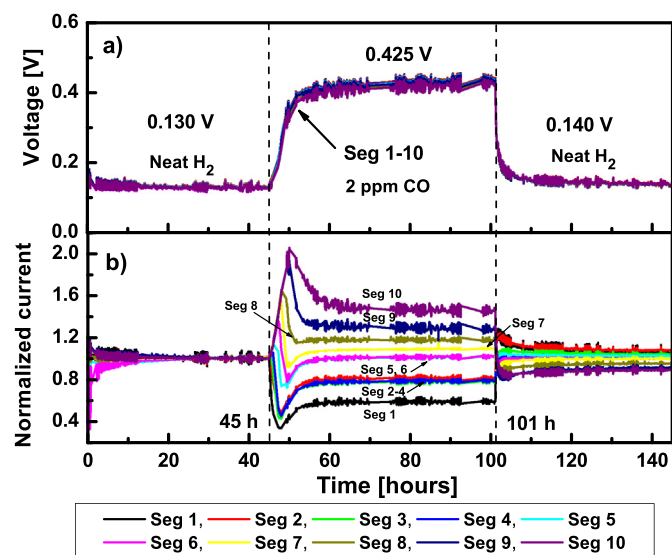
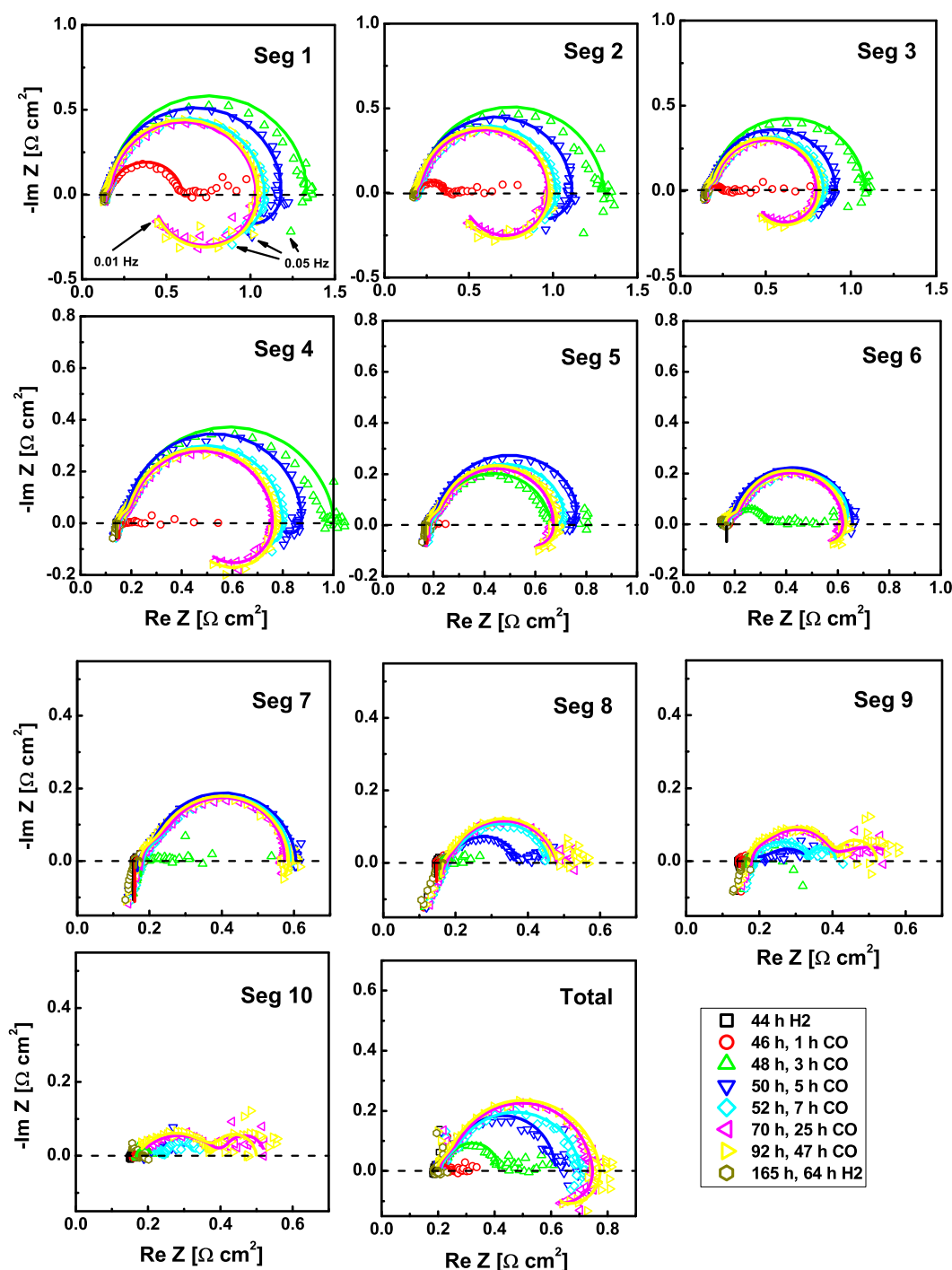


Fig. 9. Voltages (a) and current densities of each segment normalized to the initial performances (b) vs. time for an overall current density of  $0.8 \text{ A cm}^{-2}$  and a contaminant exposure of 2 ppm CO. Anode/cathode:  $H_2 + 2 \text{ ppm CO}/H_2$ ,  $0.847/0.847 \text{ l min}^{-1}$ , 100/100% RH, 48.3/48.3 kPa<sub>g</sub>, 60 °C.



**Fig. 10.** EIS for segments 1–10 and the total cell during different CO (2 ppm) exposure phases at  $0.8 \text{ A cm}^{-2}$ . Anode/cathode:  $\text{H}_2/\text{H}_2$ ,  $0.847/0.847 \text{ l min}^{-1}$ , 100/100% RH,  $60^\circ\text{C}$ ,  $48.3/48.3 \text{ kPa}$ . The experimental data are represented by symbols, and the modeling results are represented by solid lines. The spectra at 70 and 92 h were recorded up to 0.01 Hz; the others were recorded up to 0.05 Hz.

Operation at  $\text{H}_2/\text{H}_2$  gas configuration excluded any  $\text{O}_2$  presence, and CO oxidation should mainly go through the electrochemical pathway (Eqs. (52)–(56)). The anode overpotential was 0.295–0.300 V, which was lower than the ignition potential for CO electro-oxidation on Pt at  $60^\circ\text{C}$ . Yet even at lower potentials, CO electro-oxidation is still possible because the potential-dependent reaction rate constant of CO oxidation  $k(\varepsilon)$  increases with increasing electrode potential [31,106]; however, the reaction rate might be slow. At the beginning of CO exposure (1–5 h), the anode potential was still low for any CO electro-oxidation. Thus,

only CO adsorption could occur on Pt, affecting oxidation of the adsorbed hydrogen atoms and resulting in an increase of the anode charge transfer resistance ( $R_{\text{ct}, \text{a}}$ ) (Fig. 10). As soon as the segment reached its steady-state and the anode overpotential became  $\sim 0.300 \text{ V}$ , a pseudo-inductive loop appeared. The pseudo-inductive behavior could be attributed to slow CO electro-oxidation and the removal of  $\text{CO}_2$  from the Pt surface, resulting in an increase of the relaxation resistance ( $R_K$ ) and pseudo-inductance ( $L_K$ ) at the beginning of the process (Fig. 11) [31,40]. As the electrochemical oxidation of CO followed by desorption of



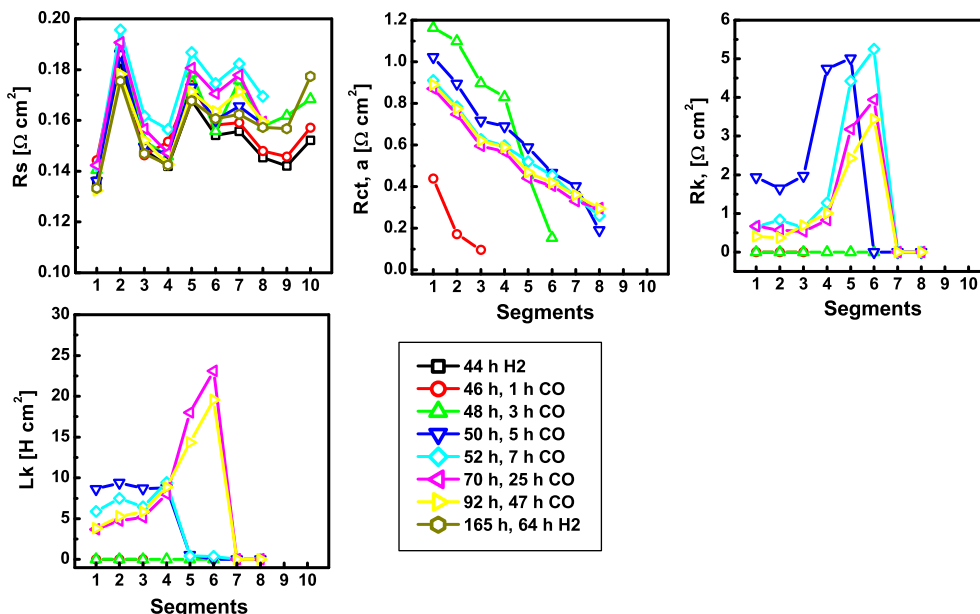


**Fig. 11.** Distributions of serial resistance ( $R_s$ ), anode charge transfer resistance ( $R_{ct,a}$ ), relaxation resistance ( $R_k$ ) and pseudo-inductance ( $L_k$ ) at various CO exposure times for  $H_2/H_2$  operation. EEC fitting was performed in the frequency range of 10 000–0.05 Hz.

$CO_2$  proceeded, it left the Pt surface vacant for hydrogen chemisorption, leading to a decrease of  $R_{ct,a}$  and  $R_k$ . This is observed in Fig. 11 as follows the initial increase of the parameters occurred at the start of poisoning.  $R_{ct,a}$ ,  $R_k$  and  $L_k$  began to decrease after 3–5 h for segments 1–4, while for segments 5 and 6 the decrease began after 7 h.

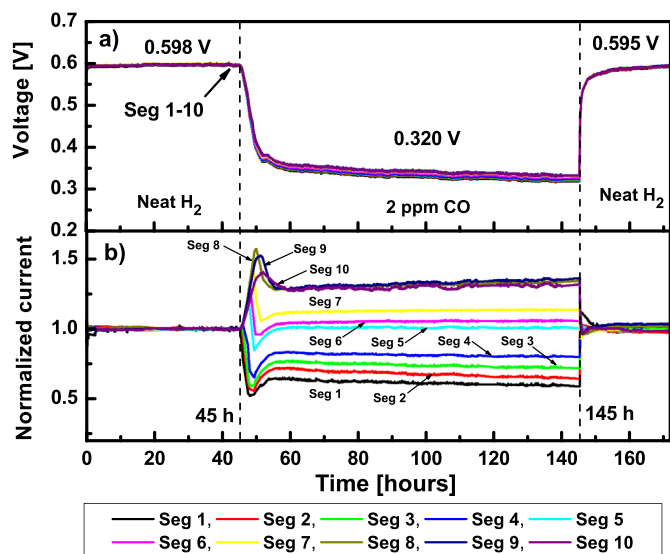
#### 4.3. Effect of CO injection during $H_2$ /air operation

Fig. 12 presents the voltage responses and normalized current densities vs. experimental time for all ten segments under  $H_2$ /air operation. A pre-poisoning period was conducted with pure  $H_2$  for the first 45 h. The segment voltages and the overall cell voltage were 0.598 V. It should be noted that using  $H_2$ /air and with an overall current density of  $0.8 \text{ A cm}^{-2}$ , diffusion control of the

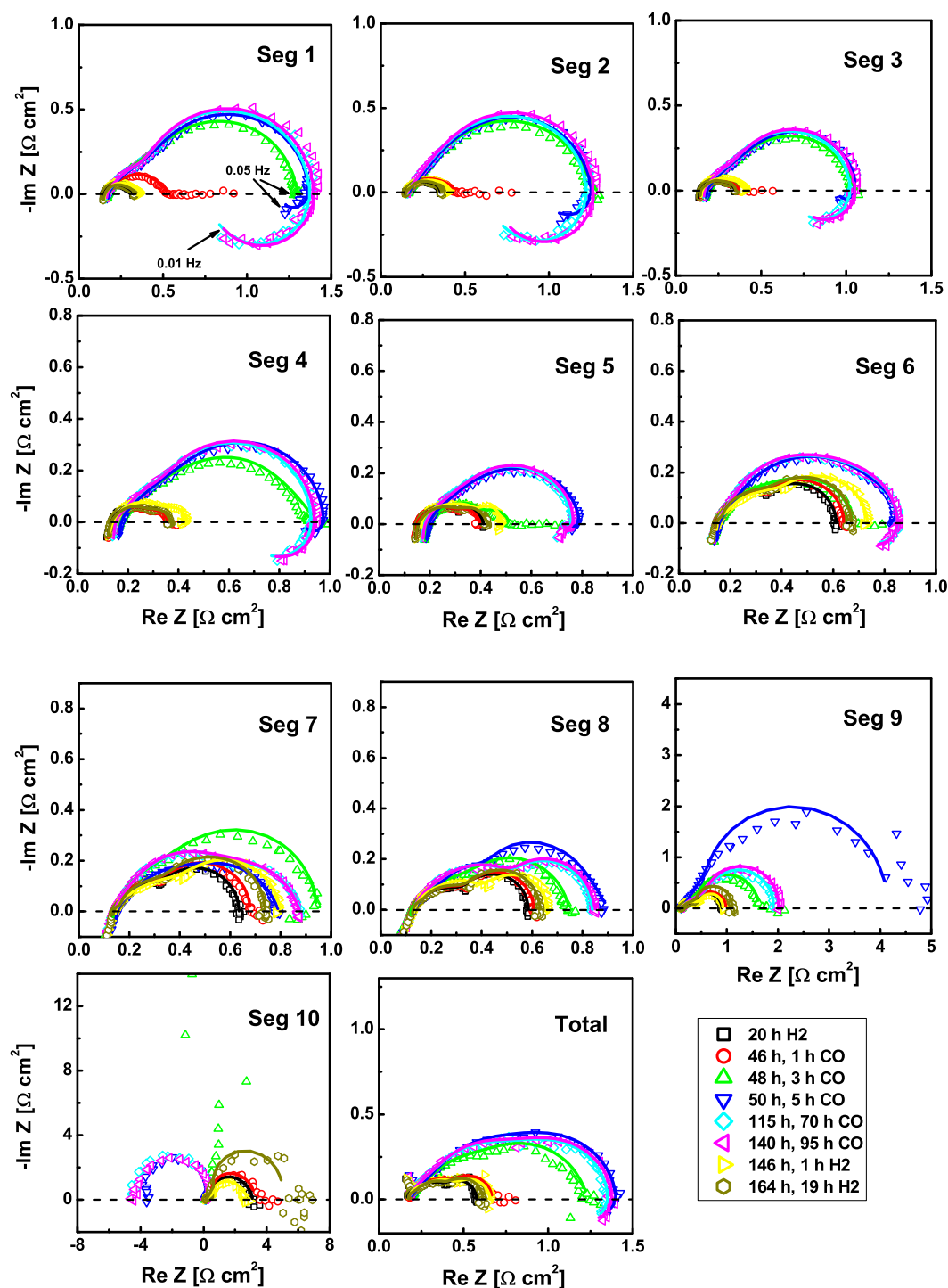
reaction in the downstream segments is more dominant vs  $H_2/O_2$  and  $H_2/H_2$  operation, especially for the outlet segments 9 and 10, which suffered from water flooding as well as the low  $O_2$  partial pressure in the gas stream. Such performance distribution at the pre-poisoning step was confirmed by spatial EIS. The injection of 2 ppm CO into the  $H_2$  stream resulted in a fast decrease in the segments' voltages and current redistribution (Fig. 12). After 7–10 h, the cell reached a steady-state with a voltage of 0.320 V. The voltage drop was  $\sim 0.280 \text{ V}$ , and the current redistribution varied in the range from  $-40\%$  to  $32\%$  from the initial segments' performance. Such changes are attributed to progressive CO poisoning of the catalyst at the inlet segments during the first hours of CO injection. The catalyst poisoning was also accompanied by a reduction of the electrochemical reaction rate and the current produced; thus, the current density of the inlet segments decreased significantly. Because the cell was operated under galvanostatic control and the overall cell current was maintained constant, there was a current increase for the outlet segments to compensate for the losses at the inlet segments. After changing the anode gas from the  $H_2 + 2 \text{ ppm CO}$  mixture to pure  $H_2$ , the cell and segments' voltages recovered to 0.595 V, and the segments' currents became similar to their initial values.

Fig. 13 presents the impedance spectra for all ten segments, the overall cell during different stages of the experiment, and the results of the EEC fitting. A comparison of the curves recorded under neat  $H_2$  operation revealed the existence of a small high-frequency anode loop, a cathode loop, and a low-frequency arc corresponding to  $O_2$  mass transfer limitations at the cathode. There was an increase in the diameter of the low-frequency loop from the inlet to the outlet, reflecting a growing diffusion limitation downstream.

A comparison of EIS curves under CO exposure revealed an increase in impedance for segments 1–3 after 1 h, while the others did not exhibit any significant changes. Such changes were attributed to progressive CO poisoning of the catalyst at the inlet segments during the first hours of the CO injection. Additionally, for these segments, a drift of the impedance values was observed at low frequency during recording of the EIS curves; this feature was similar to that observed during  $H_2/O_2$  and  $H_2/H_2$  operation.



**Fig. 12.** Voltage (a) and normalized current densities (b) of individual segments vs. time for an overall current density of  $0.8 \text{ A cm}^{-2}$  and 2 ppm CO. Anode/cathode:  $H_2$ /air,  $0.847/2.018 \text{ l min}^{-1}$ , 100/50% RH, 48.3/48.3 kPa<sub>g</sub>, 60 °C.



**Fig. 13.** EIS for segments 1–10 and the total cell during different CO (2 ppm) exposure phases at  $0.8 \text{ A cm}^{-2}$ . Anode/cathode:  $\text{H}_2/\text{air}$ ,  $0.847/2.018 \text{ l min}^{-1}$ , 100/50% RH,  $60^\circ\text{C}$ , 48.3/48.3 kPa. The experimental data are represented by symbols, and the modeling results are represented by solid lines. The spectra at 115 and 140 h were recorded up to 0.01 Hz, and the others were recorded to 0.05 Hz.

Based on the EIS data, segments 1–6 reached steady-state after 5 h of CO injection. There was an increase in HFR, the anode and cathode loops for the inlet segments. Additionally, segments 1–6 had pseudo-inductive loops in the low-frequency region, which reflects the existence of the slow process of CO oxidation involving at least one intermediate. Segments 7–9 reached steady-state several hours later. Segment 10 exhibited an increasing low-frequency loop, which finally became negative and was located in quadrant II of the Nyquist plot (Fig. 13). Such EIS behavior made EEC

fitting difficult, and segment 10 was excluded from analysis. The other segments' EIS curves could be described by the EEC depicted in Fig. 3a. EIS after 70 and 95 h of CO exposure were recorded in the frequency range of 0.01 Hz–10 kHz. The presence of the pseudo-inductive loop became pronounced for segments 1–6. Segments 7–9 did not demonstrate any inductive behavior at low frequency.

Experimental EIS measurements were performed with a time interval of several hours (2–5 h); thus, it was beneficial to evaluate the EIS evolution in detail for the first 10 h of CO exposure. For this

purpose, it was necessary to reduce the time interval between the measurements; however, it was impossible to perform EIS recording so frequently, since a certain amount of time was required (~0.5–1 h). To resolve this obstacle, cubic interpolation of

the experimental results was applied. EIS interpolation was performed in the time range from 0 to 40 000 s (0–11.11 h) with an interval of 1000 s (0.28 h). The EIS data of segment 10 are not presented here because the interpolation was not performed due to

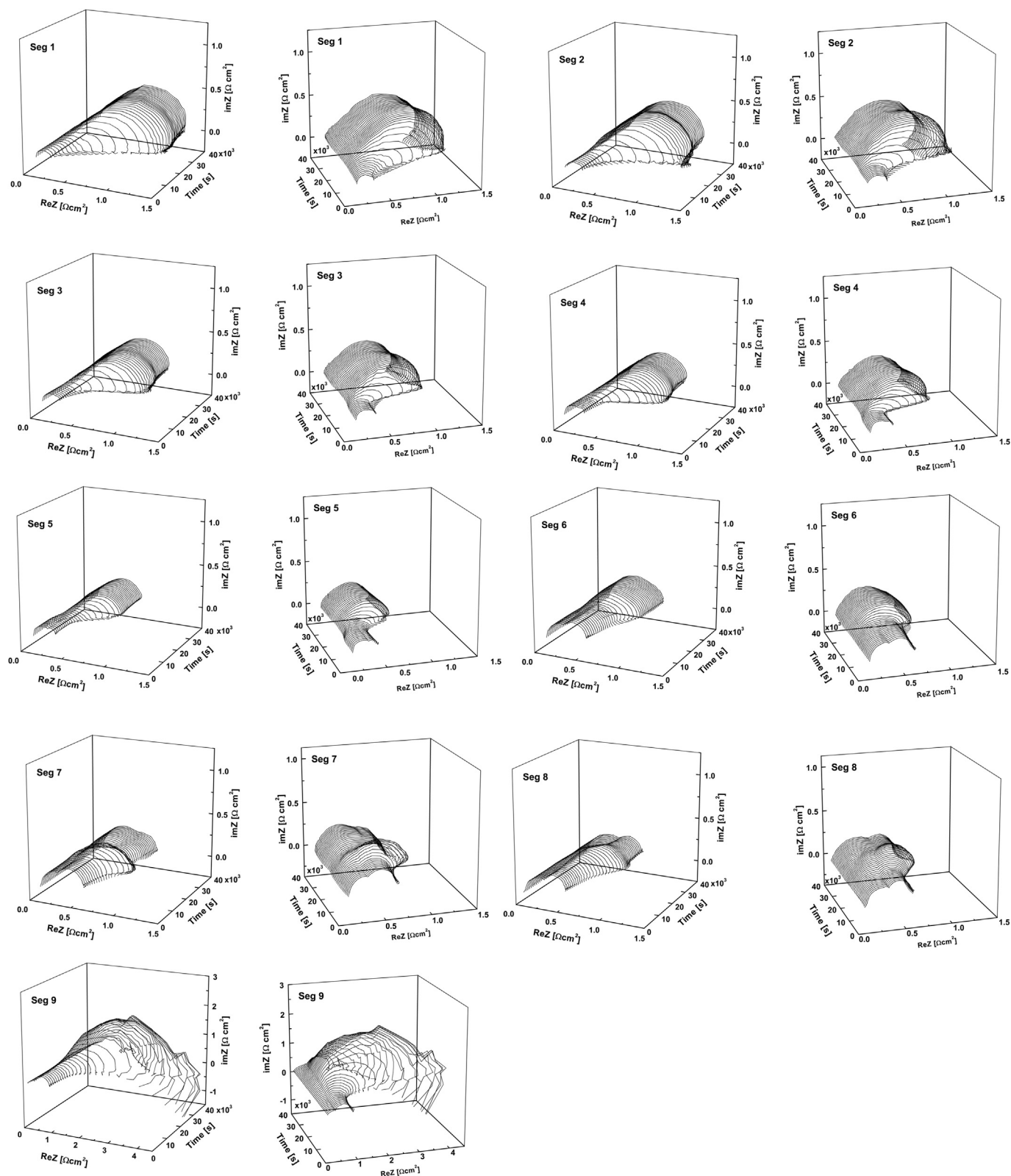


Fig. 14. Time evolution of EIS for segments 1–9 using cubic interpolation performed in the frequency range of 10 000–0.05 Hz.

the complicated nature of the recorded spectra (Fig. 13). The interpolated data profiles are presented in Fig. 14 and show the detailed temporal evolution of the impedance behavior, which could not be detected by the experimental measurements. A gradual increase of the total impedance of the segments and the development of the low-frequency pseudo-inductance can be clearly distinguished. A combination of the proposed temporal current density evolution model with the EIS interpolation approach can be a powerful tool for detailed analysis of fuel cell performance. The method can be applied for studying the effects of different operating conditions and fuel/air contaminants and for the prediction of fuel cell performance.

EEC fitting revealed that under CO exposure, there were increases in HFR, anode and cathode charge transfer resistances, as well as in the cathode Warburg resistance (Fig. 15). Analysis of the segments' EIS parameters distributions showed that the anode and cathode charge transfer resistances decreased downstream, and the effect of CO on the outlet segments decreased due to the consumption of CO by previous segments and the reduction of CO concentrations downstream. The effect of CO on segment 10 was, therefore, most likely negligibly small, and its EIS behavior may be explained by mass transfer limitations and O<sub>2</sub> depletion [63,64] instead of CO poisoning.

Operation at H<sub>2</sub>/air configuration most likely resulted in CO oxidation through chemical and electrochemical pathways (Eqs. (52)–(58)). The anode overpotential was 0.280–0.285 V, which was lower than that for H<sub>2</sub>/H<sub>2</sub> and the ignition potential for CO electro-oxidation on Pt at 60 °C. However, even at lower potential, slow CO electro-oxidation is possible as demonstrated previously [31,106]. Additionally, oxygen can diffuse from the cathode to the anode and contribute to the chemical CO oxidation (Eqs. (57) and (58)) as discussed earlier. At the beginning of CO exposure (1–5 h), adsorption of CO occurred on Pt, affecting the oxidation of the adsorbed hydrogen atoms and generated current density, which caused an increase of the anode charge transfer resistance

( $R_{ct,a}$ ) and HFR (Fig. 15) [40]. Carbon monoxide also affected the cathode and led to an increase in the cathode charge transfer resistance ( $R_{ct,c}$ ) due to uneven distributions of protonated and associated water molecules at the anode, membrane and the cathode [12,40]. In addition, there was an increase of mass transport resistance ( $R_W$ ). After 5 h of CO exposure, a pseudo-inductive loop was observed, which could be connected to slow CO electro-oxidation and removal of CO<sub>2</sub> from the Pt surface, resulting in an increase of relaxation resistance ( $R_K$ ) and pseudo-inductance ( $L_K$ ) (Figs. 13 and 15). As the electrochemical oxidation of CO proceeded, a reduction in  $R_K$  at a steady-state was also observed (Fig. 15) [31,40]. A comparison of  $R_{ct,a}$  behavior under the H<sub>2</sub>/H<sub>2</sub>, H<sub>2</sub>/O<sub>2</sub> and H<sub>2</sub>/air operating conditions (Figs. 11 and 15) revealed that the value of  $R_{ct,a}$  at H<sub>2</sub>/air is lower than that at H<sub>2</sub>/H<sub>2</sub> and higher than that of H<sub>2</sub>/O<sub>2</sub> which could be attributed to a contribution of the chemical CO oxidation to the carbon monoxide removal from the Pt anode surface. EIS of the total cell exhibited the same trend that was observed for the individual inlet segments: an increase in the impedance response and existence of a pseudo-inductive loop at low frequency.

After changing the anode gas from the H<sub>2</sub> + 2 ppm CO mixture to pure H<sub>2</sub>, the cell segments' EIS curves demonstrated significant decreases in the impedance responses, and the curves returned to their initial states after several hours of recovery.

#### 4.4. Effect of CO exposure on fuel cell performance and ECA

Fig. 16a–c presents the voltage distributions at fixed current densities as functions of the segment locations before and after the CO exposure tests performed for the different gas configurations: H<sub>2</sub>/air, H<sub>2</sub>/O<sub>2</sub> and driven H<sub>2</sub>/H<sub>2</sub>. A comparison of the curves revealed that after the first CO exposure test under H<sub>2</sub>/air conditions, the performance did not change significantly (Fig. 16a). There was a slight decrease in the performances (0.015–0.030 V) for segment 2 mainly due to ohmic losses.

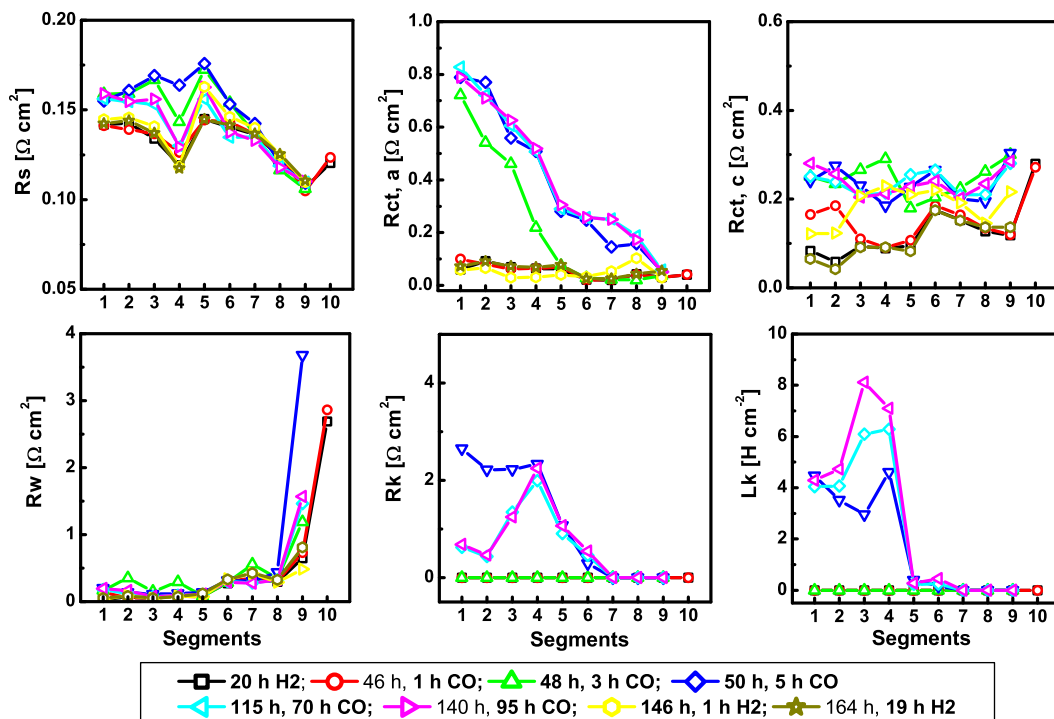
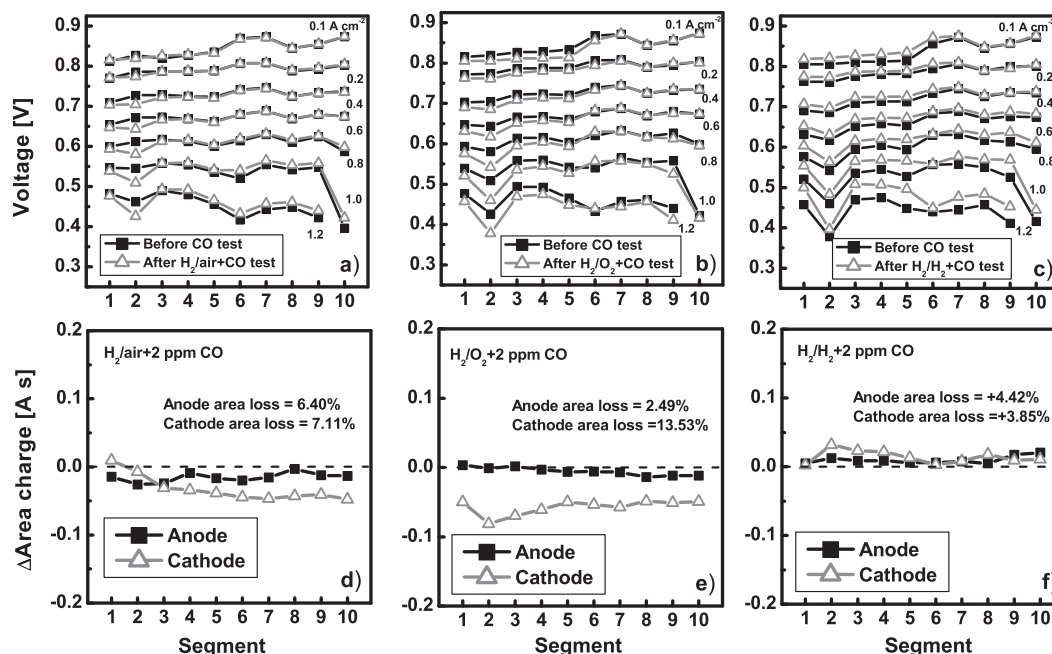


Fig. 15. Distributions of serial resistance ( $R_s$ ), anode ( $R_{ct,a}$ ) and cathode ( $R_{ct,c}$ ) charge transfer resistances, Warburg resistance ( $R_W$ ), relaxation resistance ( $R_K$ ) and pseudo-inductance ( $L_K$ ) at various CO exposure times for H<sub>2</sub>/air operation. EEC fitting was performed in the frequency range of 10 000–0.05 Hz.





**Fig. 16.** Distributions of electrochemical properties. Cell voltage distribution for various current densities up to  $1.2 \text{ A cm}^{-2}$  before and after exposure to 2 ppm CO and different oxidant gases: air (a),  $\text{O}_2$  (b) and  $\text{H}_2$  (c). Anode/cathode for performance measurements:  $\text{H}_2/\text{air}$ , 2/2 stoichiometry, 100/50% RH,  $60^\circ\text{C}$ , 48.3/48.3 kPa<sub>g</sub>. Anode and cathode ECA differences between after and before CO exposure tests performed with air (d),  $\text{O}_2$  (e) and  $\text{H}_2$  (f) as oxidants. The anode/cathode parameters for ECA measurements:  $\text{H}_2/\text{N}_2$ , 0.75/0.75 l min<sup>-1</sup>, 100/100% RH,  $35^\circ\text{C}$ , 0/0 kPa<sub>g</sub>, 20 mV s<sup>-1</sup>.

Fig. 16b shows the voltage distributions before and after the second CO exposure test under  $\text{H}_2/\text{O}_2$  conditions. The curves indicated that after the second CO test, there was a slight performance decrease (0.015–0.020 V) in inlet segments 1–4, while the others had the same performances. An analysis of the spatial performance before and after the third CO test ( $\text{H}_2 + 2 \text{ ppm CO}/\text{H}_2$ ) revealed a slight increase in the performances of segments 1–5 ( $\sim 0.025 \text{ V}$ ) over the entire current range (Fig. 16c). The observed slight performance variations demonstrated that CO exposure did not damage the MEA.

The distributions of the anode and cathode ECA differences are shown in Fig. 16d–f. The evolution of ECA after the 2 ppm CO +  $\text{H}_2/\text{air}$  test indicated that the anode and cathode losses were 6.40 and 7.11%, respectively. It should be noted that such an ECA decrease was observed during fuel cell operation without any CO exposure and might be related to typical degradation processes in occurring in new MEAs. After the CO poisoning under  $\text{H}_2/\text{O}_2$  operating conditions, a decrease of the overall cathode ECA was 13.53%, while the anode ECA decrease was only 2.49%. A similar ECA trend was previously observed in our paper [6]. The CO exposure under  $\text{H}_2/\text{H}_2$  driven test conditions resulted in a slight increase of anode and cathode ECA, which allowed us to conclude that ECA was not seriously affected during the test. After the CO test, there was no pinhole formation in the MEA, and the overall hydrogen crossover current was  $\sim 0.63 \text{ mA cm}^{-2}$ .

## 5. Conclusions

The effects of low CO concentration (2 ppm) close to the  $\text{H}_2$  fuel specification (0.2 ppm, ISO 14687-2, 2012) on spatial PEMFC performance at a constant overall cell current under  $\text{H}_2/\text{air}$ ,  $\text{H}_2/\text{O}_2$ ,  $\text{H}_2/\text{H}_2$  conditions were studied using a segmented cell system and spatial EIS. CO injection into  $\text{H}_2$  stream caused a significant current redistribution. The current densities of inlet segments 1–4 decreased, while outlet segments 7–10 demonstrated an increase

in currents. In addition, the cell voltage decreased depending on the applied cathode gas (air,  $\text{O}_2$ , or  $\text{H}_2$ ). A mathematical model from literature [9,14,29,92] was adapted to describe and understand the temporal evolution of the current density distribution under CO poisoning. The proposed simple model exhibited an adequate dynamic response of local currents during CO poisoning. This successful revelation makes the further refinement and development of the model very promising for its potential application to study the effects of other fuel/air impurities on the spatial fuel cell performance.

Spatial EIS data profiles were analyzed by EEC modeling. The results showed an increase in the HFR, anode and cathode charge transfer resistances under CO exposure. Operation with  $\text{O}_2$  as an oxidant did not result in the appearance of a pseudo-inductive loop at low frequency; moreover, the anode overpotential was only 0.085 V, which is lower than the ignition potential for CO electro-oxidation on Pt at  $60^\circ\text{C}$ . These observations allowed us to assume that the oxidation and removal of adsorbed CO occurred predominantly through a chemical pathway, where diffused  $\text{O}_2$  can directly react with CO. In contrast, operation under the  $\text{H}_2/\text{H}_2$  driven mode led to higher anode overpotential ( $\sim 0.300 \text{ V}$ ) and the existence of the pseudo-inductive loop for segments 1–6. The pseudo-inductive behavior might be attributed to a surface relaxation process of the anode including slow electrochemical reactions (CO electro-oxidation) with a single adsorbed intermediate. The lack of oxygen led to CO oxidation and removal mainly via an electro-oxidation mechanism. Using air as the feed gas at the cathode provided conditions for CO oxidation through the combination of chemical and electrochemical pathways, since the pseudo-inductance for segments 1–6 was observed, and the anode overpotential was high enough for slow CO electro-oxidation ( $\sim 0.280 \text{ V}$ ).

A comparison of the EEC parameters' distributions revealed a decrease of  $R_{\text{ct,a}}$ ,  $R_{\text{ct,c}}$ ,  $R_K$ ,  $L_K$  with the segments' location. This trend in the parameters distributions together with the lack of any

pseudo-inductive behavior for the outlet segments 7–10 under H<sub>2</sub>/air and H<sub>2</sub>/H<sub>2</sub> operating conditions allowed us to assume that CO adsorption and Pt poisoning mainly occurred at the inlet part of the cell within 5–10 h, providing dynamic responses of the segments and their spatial performance. A combination of the current distribution model with an EIS interpolation approach was demonstrated to be a powerful tool for detailed analysis and prediction of fuel cell spatial performance.

## Acknowledgments

The authors gratefully acknowledge the Office of Naval Research, United States (N00014-12-1-0496) and “Plan Promoción de la investigación UNED” (2011V/PUNED/0015 and CYCIT DPI2007-61068) for the funding of this work. The authors would also like to thank Günter Randolf for valuable support regarding solutions for the system used herein and software design as well as Jean St-Pierre for discussions concerning the data obtained. The authors are grateful to the Hawaiian Electric Company for their ongoing support of the operations of the Hawaii Sustainable Energy Research Facility.

## References

- [1] L. Carrette, K.A. Friedrich, U. Stimming, *Fuel Cells* 1 (2001) 5.
- [2] J.R. Rostrup-Nielsen, K. Aasberg-Petersen, Steam reforming, ATR, partial oxidation: catalysts and reaction engineering, in: W. Vielstich, H.A. Gasteiger, A. Lamm (Eds.), *Handbook of Fuel Cell – Fundamentals, Technology and Applications*, Fuel Cell Technology and Applications. Part 1, vol. 3, John Wiley and Sons, Weinheim, 2003, pp. 159–176 (Chapter 14).
- [3] F. Barbir, *PEM Fuel Cells: Theory and Practice*, Elsevier Academic Press, 2005.
- [4] S. Gottesfeld, J. Pafford, *J. Electrochem. Soc.* 135 (1988) 2651.
- [5] S.J. Lee, S. Mukerjee, E.A. Ticianelli, J. McBreen, Electrocatalysis of CO tolerance in hydrogen oxidation reaction in PEM fuel cells, *Electrochim. Acta* 44 (1999) 3283.
- [6] T.V. Reshetenko, K. Bethune, R. Rocheleau, *J. Power Sources* 218 (2012) 412.
- [7] H.-F. Oetjen, V.M. Schmidt, U. Stimming, F. Trila, *J. Electrochem. Soc.* 143 (1996) 3838.
- [8] J.J. Baschuk, X. Li, *Int. J. Energy Res.* 25 (2001) 695.
- [9] T.E. Springer, T. Rockward, T.A. Zawodzinski, S. Gottesfeld, *J. Electrochem. Soc.* 148 (2001) A11.
- [10] X. Cheng, Z. Shi, N. Glass, L. Zhang, J. Zhang, D. Song, Zh-Sh Liu, H. Wang, J. Shan, *J. Power Sources* 165 (2007) 739.
- [11] T.R. Ralph, M.P. Hogarth, *Platin. Metal Rev.* 46 (2002) 117.
- [12] Z. Qi, C. He, A. Kaufman, *J. Power Sources* 111 (2002) 239.
- [13] M. Murthy, M. Esayan, A. Hobson, S. MacKenzie, W.-K. Lee, J.W. Van Zee, *J. Electrochem. Soc.* 148 (2001) A1141.
- [14] J. Zhang, R. Datta, *J. Electrochem. Soc.* 149 (2002) A1423.
- [15] G.A. Camara, E.A. Ticianelli, S. Mukerjee, S.J. Lee, J. McBreen, *J. Electrochem. Soc.* 149 (2002) A748.
- [16] T. Murahashi, T. Mitsumoto, E. Nishiyama, *ECS Trans.* 25 (2009) 869.
- [17] D.J.L. Brett, P. Aguiar, N.P. Brandon, A.R. Kucernak, *Int. J. Hydrogen Energy* 32 (2007) 863.
- [18] D.L. Trimm, *Appl. Catal. A* 296 (2005) 1.
- [19] L.P.L. Carrette, K.A. Friedrich, M. Huber, U. Stimming, *Phys. Chem. Chem. Phys.* 3 (2001) 320.
- [20] W.A. Adams, J. Blair, K.R. Bullock, C.L. Gardner, *J. Power Sources* 145 (2005) 55.
- [21] W. Wang, *J. Power Sources* 191 (2009) 400.
- [22] T. Tingelöf, L. Hedström, N. Holmström, P. Alvfors, G. Lindbergh, *Int. J. Hydrogen Energy* 33 (2008) 2064.
- [23] A.A. Shah, P.C. Sui, G.-S. Kim, S. Ye, *J. Power Sources* 166 (2007) 1.
- [24] N. Zamel, X. Li, *Int. J. Hydrogen Energy* 33 (2008) 1335.
- [25] L.-Y. Sung, B.-J. Hwang, K.-L. Hsueh, W.-N. Su, C.-C. Yang, *J. Power Sources* 242 (2013) 264.
- [26] K. Ruth, M. Vogt, R. Zuber, in: W. Vielstich, H.A. Gasteiger, A. Lamm (Eds.), *Handbook of Fuel Cell – Fundamentals, Technology and Applications*, Fuel Cell Technology and Applications. Part 1, vol. 3, John Wiley and Sons, Weinheim, 2003, pp. 489–496 (Chapter 39).
- [27] T. Ioroi, K. Yasuda, Y. Miyazaki, *Phys. Chem. Chem. Phys.* 4 (2002) 2337.
- [28] S. Jiménez, J. Soler, R.X. Valenzuela, L. Daza, *J. Power Sources* 151 (2005) 69.
- [29] J. Zhang, T. Thampam, R. Datta, *J. Electrochem. Soc.* 149 (2002) A765.
- [30] M. Boaventura, H. Sander, K.A. Friedrich, A. Mendes, *Electrochim. Acta* 56 (2011) 9467.
- [31] R. Jiang, H.R. Kunz, J.M. Fenton, *J. Electrochem. Soc.* 152 (2005) A1329.
- [32] T.E. Springer, T.A. Zawodzinski, M.S. Wilson, S. Gottesfeld, *J. Electrochem. Soc.* 143 (1996) 587.
- [33] X. Yuan, H. Wang, J.C. Sun, J. Zhang, *Int. J. Hydrogen Energy* 32 (2007) 4365.
- [34] J. Wu, X.Z. Yuan, H. Wang, M. Blanco, J.J. Martin, J. Zhang, *Int. J. Hydrogen Energy* 33 (2008) 174757.
- [35] E. Barsoukov, J.R. Macdonald, *Impedance Spectroscopy Theory, Experiment, and Applications*, John Wiley & Sons, 2005.
- [36] B. Müller, N. Wagner, W. Schnurnberger, Change of electrochemical impedance spectra with time during CO-poisoning of the Pt anode in a membrane fuel cell, in: S. Gottesfeld, T.F. Fuller (Eds.), *Proton Conducting Membrane Fuel Cell II*, 1999, pp. 187–199. *Electrochem. Soc. Proc.* 98027.
- [37] M. Ciureanu, H. Wang, *J. Electrochem. Soc.* 146 (1999) 4031.
- [38] C.A. Schiller, F. Richter, E. Gülzow, N. Wagner, *Phys. Chem. Chem. Phys.* 3 (2001) 2113.
- [39] N. Wagner, M. Schulze, *Electrochim. Acta* 48 (2003) 3899.
- [40] N. Wagner, E. Gülzow, *J. Power Sources* 127 (2004) 341.
- [41] M. Ciureanu, H. Wang, Z. Qi, *J. Phys. Chem. B* 103 (1999) 9645.
- [42] M. Ciureanu, H. Wang, *J. New Mat. Electrochem. Syst.* 3 (2000) 107.
- [43] X. Wang, I.-M. Hsing, Y.-J. Leng, P.-L. Yue, *Electrochim. Acta* 46 (2001) 4397.
- [44] J.-D. Kim, Y.-I. Park, K. Kobayashi, M. Nagai, *J. Power Sources* 103 (2001) 127.
- [45] Y.-J. Leng, X. Wang, I.-M. Hsing, *J. Electroanal. Chem.* 528 (2002) 145.
- [46] F. Hajbolouri, B. Andreau, G.G. Scherer, A. Wokaun, *Fuel Cells* 4 (2004) 160.
- [47] M.-C. Yang, *J. Electrochem. Soc.* 153 (2006) A1043.
- [48] A.K. Meland, S. Kjelstrup, *J. Electroanal. Chem.* 610 (2007) 171.
- [49] M.A. Rubio, A. Urquia, S. Dormido, *Int. J. Hydrogen Energy* 35 (2010) 2586.
- [50] Y. Tang, H. Zhang, H. Zhong, Z. Xu, *Int. J. Hydrogen Energy* 37 (2012) 2129.
- [51] J.T. Müller, P.M. Urban, W.F. Hölderich, *J. Power Sources* 84 (1999) 157.
- [52] Y.-C. Liu, X.-P. Qiu, W.-T. Zhu, G.-S. Wu, *J. Power Sources* 114 (2003) 10.
- [53] D. Chakraborty, I. Chorkendorff, T. Johannessen, *J. Power Sources* 162 (2006) 1010.
- [54] C.A. Schiller, F. Richter, E. Gülzow, N. Wagnere, *Phys. Chem. Chem. Phys.* 3 (2001) 374.
- [55] L.C. Pérez, L. Brandão, J.M. Sousa, A. Mendes, *Renew. Sustain. Energy Rev.* 15 (2011) 169.
- [56] S. Cleghorn, C.R. Derouin, M.S. Wilson, S. Gottesfeld, *J. Appl. Electrochem.* 28 (1998) 663.
- [57] J. Stumper, S.A. Campbell, D.P. Wilkinson, M.C. Johnson, M. Davis, *Electrochim. Acta* 43 (1998) 3773.
- [58] M. Noponen, T. Mennola, M. Mikkola, T. Hottinen, P. Lund, *J. Power Sources* 106 (2002) 304.
- [59] J.J. Hwang, W.R. Chang, R.G. Peng, P.Y. Chen, A. Su, *Int. J. Hydrogen Energy* 33 (2008) 5718.
- [60] Y.-G. Yoon, W.-Y. Lee, T.-H. Yang, G.-G. Park, *J. Power Sources* 118 (2003) 193.
- [61] R.N. Büchi, A.B. Geiger, R.P. Neto, *J. Power Sources* 145 (2005) 62.
- [62] F.-B. Weng, B.-Sh. Jou, Ch.-W. Li, A. Su, Sh.-H. Chan, *J. Power Sources* 181 (2008) 251.
- [63] I.A. Schneider, S.A. Freunberger, D. Kramer, A. Wokaun, G.G. Scherer, *J. Electrochem. Soc.* 154 (2007) B383.
- [64] I.A. Schneider, D. Kramer, A. Wokaun, G.G. Scherer, *J. Electrochem. Soc.* 154 (2007) B770.
- [65] D.G. Sanchez, P.L. Garcia-Ybarra, *Int. J. Hydrogen Energy* 37 (2012) 7279.
- [66] M. Schulze, E. Gülzow, St. Schönbauer, T. Knori, R. Reissner, *J. Power Sources* 173 (2007) 19.
- [67] D. Spornjak, J. Fairweather, R. Mukundan, T. Rockward, R.L. Borup, *J. Power Sources* 214 (2012) 386.
- [68] T.V. Reshetenko, G. Bender, K. Bethune, R. Rocheleau, *Electrochim. Acta* 56 (2011) 8700.
- [69] T.V. Reshetenko, G. Bender, K. Bethune, R. Rocheleau, *Electrochim. Acta* 69 (2012) 220.
- [70] R. Lin, E. Gülzow, M. Schulze, K.A. Friedrich, *J. Electrochem. Soc.* 158 (2011) B11.
- [71] T.V. Reshetenko, G. Bender, K. Bethune, R. Rocheleau, *Electrochim. Acta* 76 (2012) 16.
- [72] T.V. Reshetenko, G. Bender, K. Bethune, R. Rocheleau, *Electrochim. Acta* 80 (2012) 368.
- [73] T.V. Reshetenko, J. St-Pierre, R. Rocheleau, *J. Power Sources* 241 (2013) 597.
- [74] R. Borup, R. Mukundan, J. Davey, J. Spendelov, P. Mukherjee, D. Wood, M. Nelson, F. Garzon, M. Arif, D. Jacobson, D. Hussey, In situ PEM fuel cell water managements, LRD42b-3, 2009 Fuel Cell Seminar, November 16–19, 2009, Palm Springs, CA, USA.
- [75] L.C. Pérez, J. Ihonon, J.M. Sousa, A. Mendes, *Fuel Cells* 13 (2013) 203.
- [76] A. Lamibrac, G. Maranzana, O. Lottin, J. Mainka, S. Didierjean, A. Thomas, C. Moyne, *J. Power Sources* 196 (2011) 9451.
- [77] D. Liang, Q. Shen, M. Hou, Z. Shao, B. Yi, *J. Power Sources* 194 (2009) 847.
- [78] M. Dou, M. Hou, Q. Shen, H. Znaheb, W. Lu, Z. Shao, B. Yi, *J. Power Sources* 196 (2011) 2759.
- [79] Z. Liu, L. Yang, Z. Mao, W. Zhuge, Y. Zhang, L. Wang, *J. Power Sources* 157 (2006) 166.
- [80] S. Kirsch, R. Hanke-Rauschenbach, B. Stein, R. Kraume, K. Sundmacher, *J. Electrochem. Soc.* 160 (2013) F436.
- [81] Ch Wieser, A. Helmbold, E. Gülzow, *J. Appl. Electrochem.* 30 (2000) 803.
- [82] G. Bender, M.S. Wilson, T.A. Zawodzinski, *J. Power Sources* 123 (2003) 163.
- [83] J.E.B. Randles, *Discuss. Faraday Soc.* 1 (1947) 11.
- [84] N. Fouquet, C. Doulet, C. Nouillant, G. Dauphin-Tanguy, B. Ould-Bouamama, *J. Power Sources* 159 (2006) 905.
- [85] Z. Xie, S. Holdcroft, *J. Electroanal. Chem.* 568 (2004) 247.
- [86] K.S. Cole, R.H. Cole, *J. Chem. Phys.* 9 (1941) 341.

- [87] V.A. Alves, L.A. da Silva, J.F.C. Boodts, *Electrochim. Acta* 44 (1998) 1525.
- [88] J.R. Macdonald, *Phys. Rev.* 92 (1953) 4.
- [89] D.A. Harrington, B.E. Conway, *Electrochim. Acta* 32 (1987) 1703.
- [90] M.A. Rubio, A. Urquia, S. Dormido, *J. Power Sources* 171 (2007) 670.
- [91] J. Zhang, J.D. Fehribach, R. Datta, *J. Electrochem. Soc.* 151 (2004) A689.
- [92] T. Kadyk, S. Kirsch, R. Hanke-Rauschenbach, K. Sundmacher, *Electrochim. Acta* 56 (2011) 10593.
- [93] T. Kadyk, S. Kirsch, R. Hanke-Rauschenbach, K. Sundmacher, *J. Appl. Electrochem.* 41 (2011) 1021.
- [94] P. Gode, G. Lindbergh, G. Sundholm, *J. Electroanal. Chem.* 518 (2002) 115.
- [95] D.A. Crespo-Yapur, A. Bonnefont, R. Schuster, K. Krischer, E.R. Savinova, *Chem. Phys. Chem.* 14 (2013) 1117.
- [96] R. Makharia, M.F. Mathias, D.R. Baker, *J. Electrochem. Soc.* 152 (2005) A970.
- [97] M. Cimenti, M. Tam, J. Stumper, *Electrochem. Solid-State Lett.* 12 (2009) B131.
- [98] N.V. Dale, M.D. Mann, H. Salehfar, A.M. Dhirde, T. Han, *J. Fuel Cell Sci. Tech.* 7 (2010) 031010.
- [99] X. Yuan, J.C. Sun, M. Blanco, H. Wang, J. Zhang, D.P. Wilkinson, *J. Power Sources* 161 (2006) 920.
- [100] X. Yuan, J.C. Sun, H. Wang, J. Zhang, *J. Power Sources* 161 (2006) 929.
- [101] K.J. Vetter, *Electrochemical Kinetics*, Academic Press, New York, London, 1967, p. 516.
- [102] N.R. Elezović, Lj. Gajić-Krstajić, V. Radmilović, Lj. Vračar, N.V. Krstajić, *Electrochim. Acta* 54 (2009) 1375.
- [103] S. Gilman, *J. Phys. Chem.* 68 (1964) 70.
- [104] N.M. Markovic, T.J. Schmidt, B.N. Grgur, H.A. Gasteiger, R.J. Behm, P.N. Ross, *J. Phys. Chem. B* 103 (1999) 8568.
- [105] N.M. Markovic, C.A. Lucas, B.N. Grgur, P.N. Ross, *J. Phys. Chem. B* 103 (1999) 9616.
- [106] H.A. Gasteiger, N.M. Markovic, P.N. Ross, *J. Phys. Chem.* 99 (1995) 8290.
- [107] T. Gu, W.-K. Lee, J.W. Van Zee, *Appl. Catal. B* 56 (2005) 43.
- [108] H.P. Dhar, L.G. Christner, A.K. Kush, H.C. Maru, *J. Electrochem. Soc.* 133 (1986) 1571.
- [109] H.P. Dhar, L.G. Christner, A.K. Kush, *J. Electrochem. Soc.* 134 (1987) 3021.